HOKKAIDO UNIVERSITY

Title	Electron Spin Resonance Studies of Molecular Mott Insulators with Triangular Lattice
Author(s)	Kim, Sunghyun
Degree Grantor	北海道大学
Degree Name	博士(理学)
Dissertation Number	甲第13557号
Issue Date	2019-03-25
DOI	https://doi.org/10.14943/doctoral.k13557
Doc URL	https://hdl.handle.net/2115/74232
Type	doctoral thesis
File Information	Kim_Sunghyun.pdf

Hokkaido University Collection of Scholarly and Academic Papers : HUSCAP

Doctoral Thesis

Electron Spin Resonance Studies of Molecular Mott Insulators with Triangular Lattice

Kim Sunghyun

Department of Condensed Matter Physics, Graduate School of Science, Hokkaido University

March 2019

Contents

1 Introduction **2**

1.1 Molecular-based triangular lattice system 2

1.2 Ground states of the antiferromagnetic triangular lattice system 10

1.3 The molecular-based triangular lattice system $X[Pd(dmit)_2]_2$ 14

1.3.1 The X = Me_4P, Et_2Me_2P, Me_4Sb salts (Antiferromagnetic state) 17

1.3.2 The X = $EtMe_3Sb$ salt (Quantum spin liquid state) 18

1.3.3 The X = Et_2Me_2Sb salt (Charge-ordered state) 21

1.3.4 The X = $EtMe_3P$ salt (The Valence Bond Solid state) 23

1.4 Motivations of this study 26

1.5 Experimental methods 28

1.5.1 The sample information 28

1.5.2 Electron Spin Resonance 29

1.5.3 Sample setup for X-band ESR 31

1.5.4 Sample setup for V- and W-band ESR 32

1.5.5 Spin counting method 34

2 Results and Discussions **36**

2.1 The X = Me_4P, Et_2Me_2P, Me_4Sb, $EtMe_3Sb$, Et_2Me_2Sb salts 36

2.1.1 The ESR measurement results 36

2.1.2 Discussions 47

2.2 The X = $EtMe_3P$ salt (The valence bond solid state) 50

2.2.1 The ESR measurement results 50

2.2.2 Discussions 58

3 Conclusion **62**

Chapter 1

Introduction

1.1 Molecular-based triangular lattice system

The antiferromagnetic triangular lattice is an interesting system since it exhibits various ground states due to the geometrical frustration. If antiferromagnetic spins are located on the edges of the square lattice, spins can be aligned antiparallel with its neighbour spins, and antiferromagnetic Néel order can occur (Fig. 1.1(a)). Then, what happens if the antiferromagnetic spins are located on the edges of the triangular lattice? In that case, the first two spins can be aligned antiparallel, but the third spin state becomes frustrated since it cannot be aligned antiferromagnetically because two spin orientations are possible (Fig. 1.1(b)). In a such situation, the low-energy levels are degenerated, and the quantum fluctuation is enhanced. This is known as the geometrical frustration, and the enhancement of the quantum fluctuation will affect the magnetic ground state of the system. [1]

In 1973, Anderson proposed for the first time the spin liquid state in a triangular lattice, which is a state of matter where the spins are correlated, yet fluctuate strongly even at low temperature. [2] The fluctuation is so strong that there is no long-range order for the spin liquid state. The ground states of such antiferromagnetic triangular lattice materials have been actively studied since then.

At first, inorganic triangular lattice materials, such as ABX_3 type compounds (A=Cs, Rb$\cdots$, B=Cu, Ni, C, Fe$\cdots$, X=Cl, Br) have been studied. [3, 4] Among them, $CsCuCl_3$ has been intensively studied. The spin is located on the Cu^{2+} ion ($S = 1/2$), and the Cu^{2+} ions form the triangular lattice. However, it turns out that the $CsCuCl_3$ has the Néel order

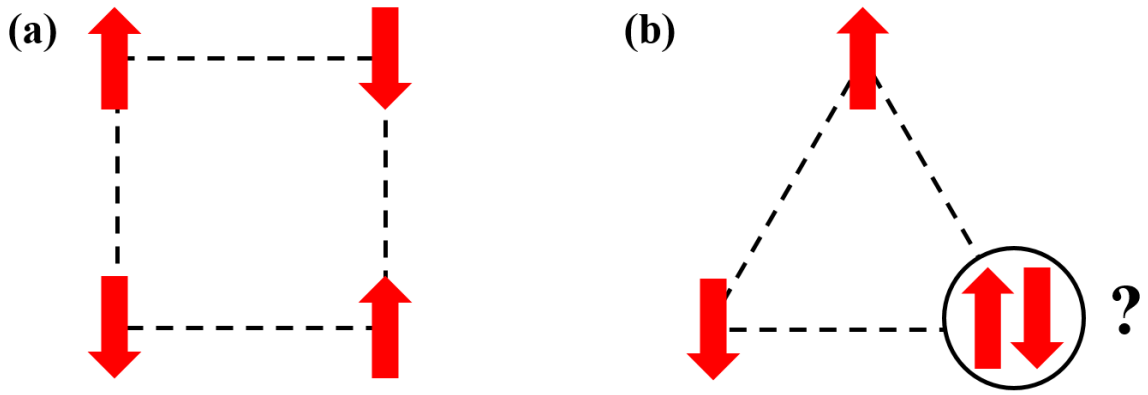

Figure 1.1: The antiferromagnetic (a) square lattice and (b) triangular lattice.

state (120° order) at 10.7 K, and not the spin liquid state. [5,6]

Recently, spin liquid candidate material $YbMgGaO_4$ has been recently found. [7] In $YbMgGaO_4$, Yb^{3+} ($S = 1/2$) forms the triangular lattice. This sample is considered to have a spin liquid ground state from the heat capacity and neutron scattering measurements. [8,9] However, there are disorder at the Mg^{2+} and Ga^{3+} sites, which are irrelevant to the triangular lattice, but the disorder may influence the exchange interaction of the triangular lattice, and may induce the spin liquid state.

On the other hand, several molecular-based antiferromagnets, which consist of triangular lattice, have been recently found. Among them, κ-$(BEDT\text{-}TTF)_2Cu_2(CN)_3$ is one of the candidate materials for the spin liquid ground state. [10] This sample consists of two donor molecules BEDT-TTF and a counter anion $Cu_2(CN)_3$. The BEDT-TTF molecule is shown in Fig. 1.2. Two BEDT-TTF molecules form a dimer and the dimers are stacked as shown in Fig. 1.3(a). Since the anion $Cu_2(CN)_3$ is monovalent, the charge is +0.5e per BEDT-TTF molecule. however, this system is an insulator due to the dimerization of the BEDT-TTF molecules and the strong on-site Coulomb repulsion. Namely, the band filling becomes effective half-filled due to the dimerization, and the system is a Mott insulator because of the strong Coulomb repulsion.

Since this system is a Mott insulator, there is one localized electron ($S = 1/2$) on the BEDT-TTF dimer. Moreover, these BEDT-TTF dimers form a triangular lattice as shown in Fig. 1.3(a). Hence, this system can be treated as a $S = 1/2$ triangular lattice. The anisotropy of the triangular lattice in this system is treated from the intradimer transfer integrals as

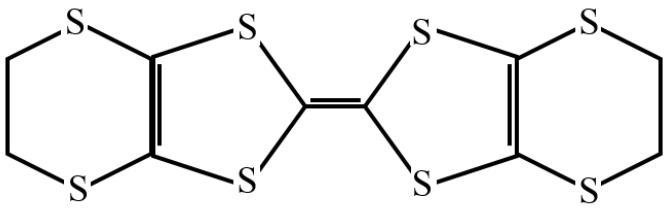

Figure 1.2: Schematic illustration of BEDT-TTF molecule.

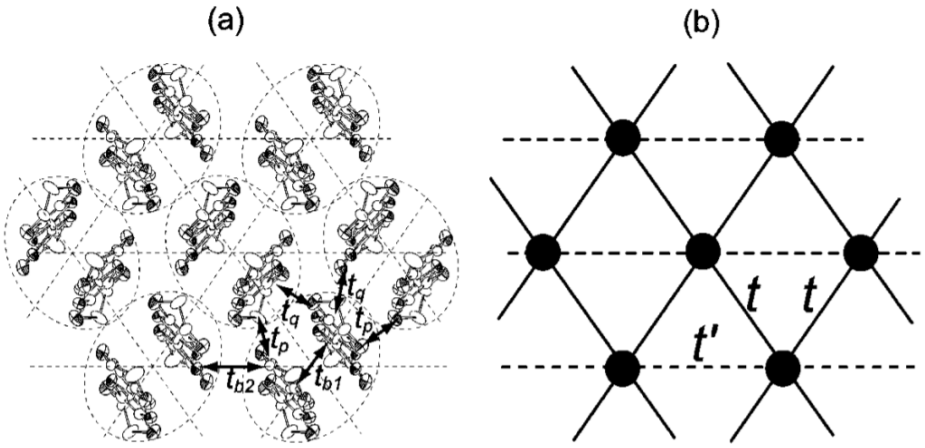

Figure 1.3: (a) Crystal structure of κ-(BEDT-TTF)$_2$Cu$_2$(CN)$_3$ (b) Schematic representation of the electronic structure of κ-(BEDT-TTF)$_2$X (X is monovalent anion), where the dots represent the BEDT-TTF dimer units. [11]

shown in Fig. 1.3(b). The anisotropic ratio t'/t of the antiferromagnetic triangular lattice is $t'/t = 1.06$, where the nearest neighbor transfer is t and the second-nearest neighbor transfer is t' (Fig. 1.3(b)). The anisotropic ratio t'/t is close to the unity, and it can be considered as a regular triangular lattice, and the geometrical frustration should work against the antiferromagnetic long-range ordering.

Figure 1.4 is ^{1}H NMR spectra for κ-(BEDT-TTF)$_2$Cu$_2$(CN)$_3$. [11] The NMR spectra do not show a drastic change down to the lowest temperature. This result indicates that there is no long-range order down to 32 mK. Meanwhile, heat capacity and thermal conductivity provide information about the low-energy excitation. Figure 1.5 is the results of heat capacity for κ-(BEDT-TTF)$_2$Cu$_2$(CN)$_3$. [12] This result shows a finite T-linear term at the zero-temperature limit. This is a surprising result since this system is an insulator. The T-linear term suggests the existence of deconfined spins, which is expected for the excited state

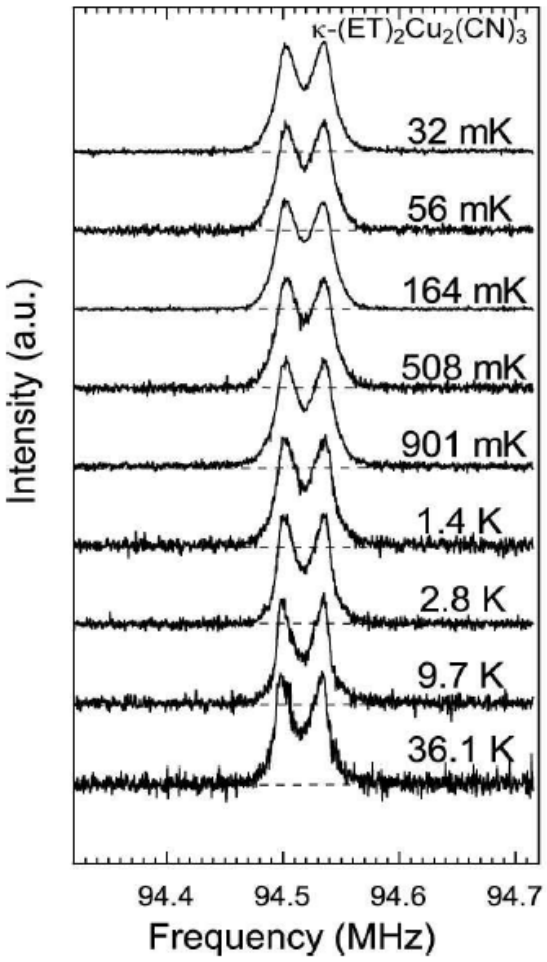

Figure 1.4: ^{1}H NMR spectra for single crystals of κ-(BEDT-TTF)$_2$Cu$_2$(CN)$_3$. [11]

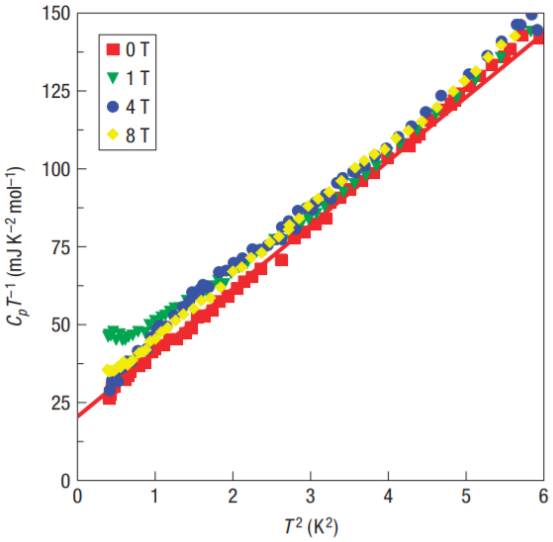

Figure 1.5: Low-temperature heat capacities C_p for κ-(BEDT-TTF)$_2$Cu$_2$(CN)$_3$ plotted in C_p/T versus T^2. [12]

of the spin liquid state. Hence, this result indicates that the system has a spin liquid ground state.

Moreover, the finite T-linear term suggests that the spin excitation is gapless. However, temperature dependence of the thermal conductivity measurement didn't observe the finite T-linear term, which indicates a gapped spin excitation (Fig. 1.6). [13] This result is in contradiction with the heat capacity measurements, which claims the presence of gapless spin excitations. Thus, there are still strong debates in this system whether the spin liquid state is gapped or gapless.

κ-(BEDT-TTF)$_2$Ag$_2$(CN)$_3$ is also a candidate for the spin liquid state. The anisotropic ratio t'/t of the antiferromagnetic triangular lattice is $t'/t = 0.9$. The NMR spectra results indicate that there is no long-range order down to 0.11 K (Fig. 1.7). [14] As shown in Fig. 1.8 specific heat measurement shows also a T-linear term in the zero-temperature limit. Therefore, κ-(BEDT-TTF)$_2$Ag$_2$(CN)$_3$ is also expected to have gapless spin liquid state.

Meanwhile, κ-H$_3$(Cat-EDT-TTF)$_2$ is considered to have also the spin liquid ground state from heat capacity measurement. [15] The heat capacity measurementalso shows T-linear term in the zero-temperature limit as shown in Fig. 1.9. [15]

The anion radical salts X[Pd(dmit)$_2$]$_2$ are also a system which consists of a triangular lattice. [16, 17] Here, X is a monovalent cation. Among them, the X = EtMe$_3$Sb salt is also a

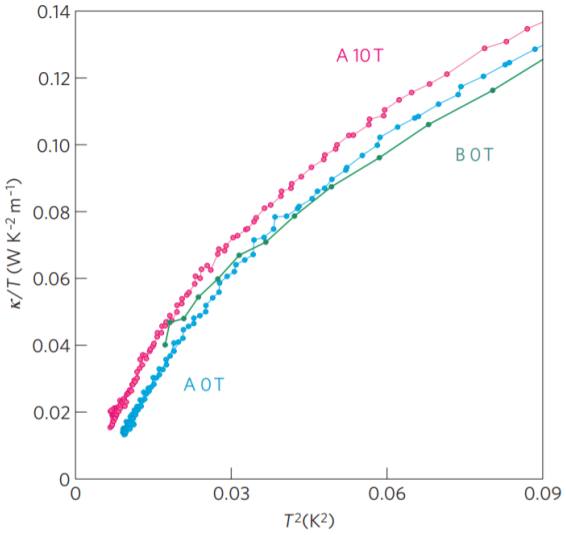

Figure 1.6: Low-temperature thermal conductivity κ-(BEDT-TTF)$_2$Cu$_2$(CN)$_3$ plotted in κ/T versus T^2. [13]

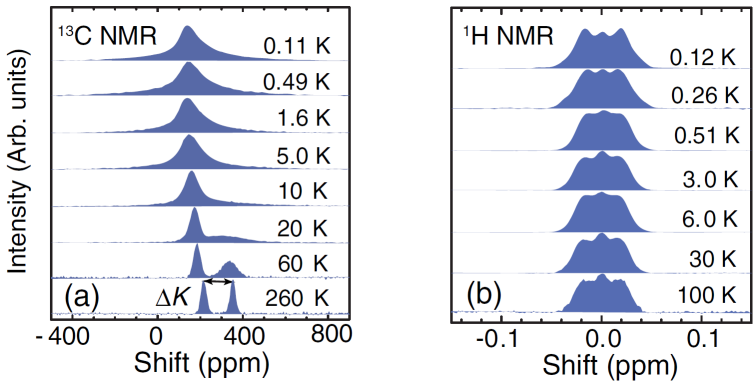

Figure 1.7: (a) ^{13}C (8.5 T) and (b) ^{1}H (2.0 T) NMR spectra for κ-(BEDT-TTF)$_2$Ag$_2$(CN)$_3$. [14]

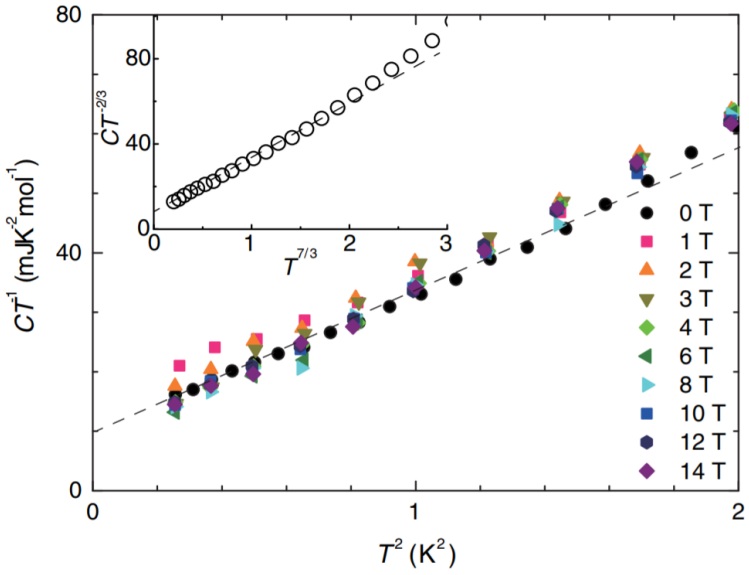

Figure 1.8: Low-temperature specific heat C for κ-(BEDT-TTF)$_2$Ag$_2$(CN)$_3$ plotted in C/T versus T^2. [14]

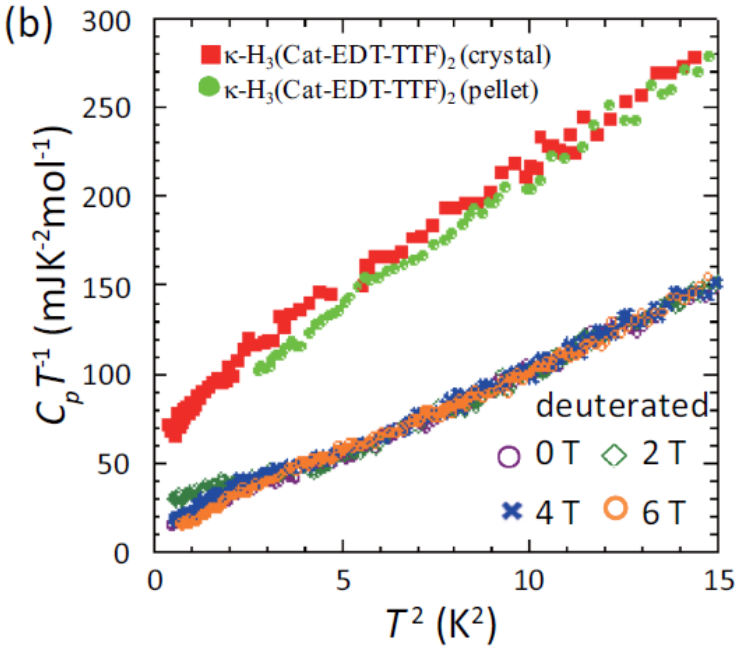

Figure 1.9: Low-temperature heat capacitie C_p for κ-H$_3$(Cat-EDT-TTF)$_2$ plotted in C_p/T versus T^2. [15]

candidate material for the spin liquid ground state. [16]

The NMR spectra indicate that there is no long-range order down to 19.4 mK. [16] And heat capacity and thermal conductivity measurement show a T-linear term in the zero-temperature limit. [18, 19] Therefore, $EtMe_3Sb[Pd(dmit)_2]_2$ is expected to have a gapless spin liquid ground state. The details will be presented in the following section 1.3.

Although the $EtMe_3Sb[Pd(dmit)_2]_2$ salt shows the the spin liquid ground state, other $X[Pd(dmit)_2]_2$ salts with different monovalent cation X shows a different magnetic ground state. And the different ground state appears because of the different geometrical frustration for each salt. [16] Due to such feature, $X[Pd(dmit)_2]_2$ is interesting system material to investigate the effect of geometric frustration in the triangular lattice.

$X[Pd(dmit)_2]_2$ system has the advantage of being able to control anisotropy of triangular lattice through the molecular modification. But molecular-based materials are very small and contain lots of protons, and it is difficult to perform neutron scattering measurement. Thus, it needs other measurements for investigating the ground states.

In the next section, the ground state of the antiferromagnetic triangular lattice system will be introduced.

	Order parameter	Presence or absence of the spin-gap	First excitation
Néel order	Staggered moment	gapless	magnon
Valence Bond Solid (VBS)	S=0 dimer-dimer correlation	gapped C activation-type χ activation-type	Confined spinon
Short-range RVB	No order parameter	gapped C activation-type χ activation-type	Deconfined spinon
Long-range RVB	No order parameter	S=0 gapless, S=1 gapped C finite (independent of H) χ activation-type	Deconfined spinon T=0 residual entropy
Spinon Fermi surface	No order parameter	gapless C = γT (?) χ Finite	Deconfined (free) spinon + gauge field

Figure 1.10: The summary of ground states of triangular lattice. [20]

1.2 Ground states of the antiferromagnetic triangular lattice system

The table in Fig. 1.10 shows several ground states proposed for the antiferromagnetic triangular lattice. [20] The antiferromagnetic triangular lattice can be described from the Heisenberg model

$$\mathcal{H} = J \sum_{<i,j>} \boldsymbol{S}_i \cdot \boldsymbol{S}_j \tag{1.1}$$

where J > 0, and $<i,j>$ refers to the nearest-neighbour pairs of the triangular lattice.

It is considered that the classical antiferromagnetic triangular lattice system has 120° order state (Néel order state) as shown in Fig. 1.11(a). In the 120° order state, spins are aligned as shown in Fig. 1.11(a) so that the total energy is minimized, and the antiferromagnetic long-range order appears. Since it is antiferromagnetically long-range ordered, the first spin excitation is a spin-wave excitation (i.e. magnon), and is gapless.

Another proposed ground state for the triangular lattice is the valence bond solid (VBS) state as shown in Fig. 1.11(b), where two spins form a singlet. The VBS state can also be accompanied by the breaking of lattice symmetry. The VBS state is similar to the spin-Peierls system which is observed in the one-dimensional antiferromagnetic spin system. [21–23] The

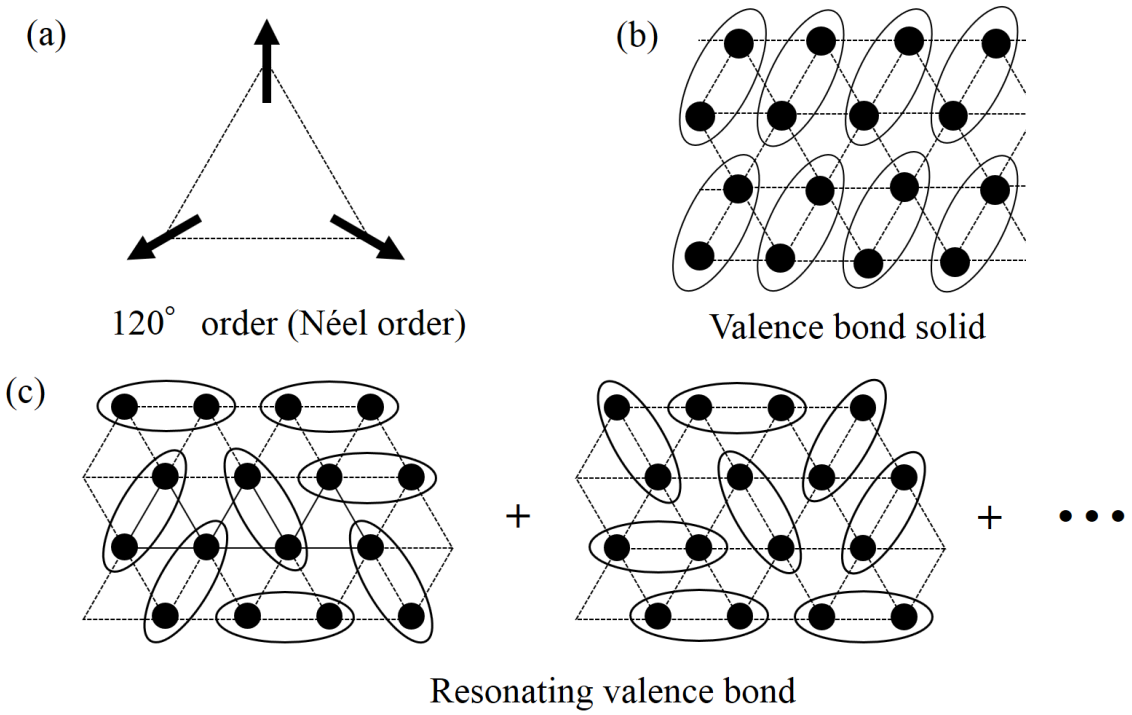

Figure 1.11: Schematic of the ground states of triangular lattice. (a) The 120° order (Néel order), (b) The valence bond solid (c) The resonating valence bond

nature of the elementary excitations for the VBS state remains an open question. [24] The creation of two spins by breaking the valence bond (or the triplet state) is certainly the basic mechanism of the spin excitation of the VBS state. It is considered that the energy cost of the two separated spins will increase with its distance since such separated spins need to create staggered valence bond(s) (Fig. 1.12), and the staggered valence bond requires more energy cost. Such energy cost might work as an elastic restoring force for binding the two spins (even for defect spins). For this reason, it is believed that the first spin excitations of the VBS state should be S=1 bosons, but unexpected low-energy spin excitations might exist. [24] Besides the S=1 triplet excitations, exotic spin excitations, such as soliton excitation or collective spin excitation, have been observed in the spin-Peierls systems. [25, 26] The VBS state becomes non-magnetic below the transition temperature (T_{VBS}), since valence bonds (spin singlets) are formed. Meanwhile, the heat capacity is expected to go to zero since the VBS state is gapped (i.e. activation-type specific heat).

The resonating valence bonds (RVB) state is introduced by Anderson in 1973. [2] The RVB state can be viewed as a linear superposition of disordered valence bond configurations

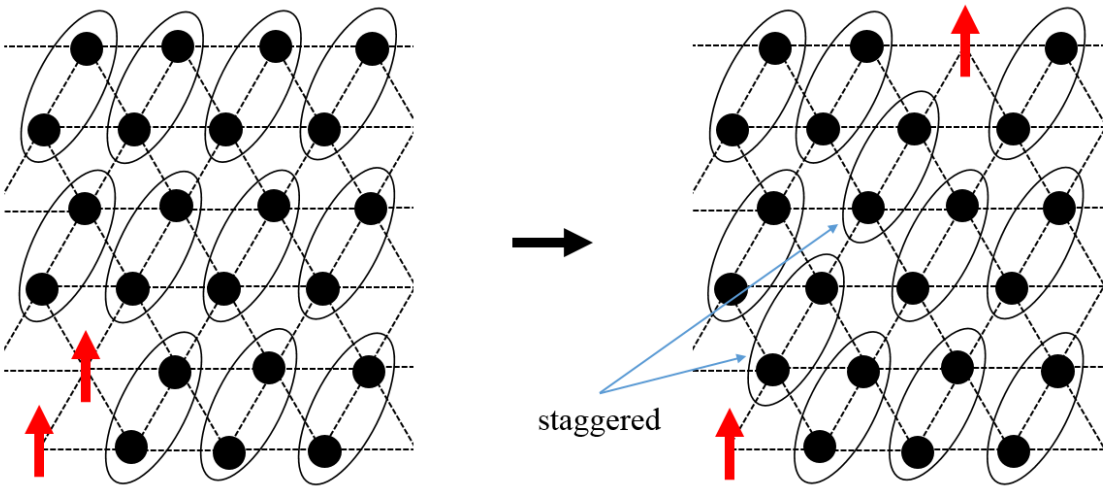

Figure 1.12: Breaking of a valence bond results in two spin excitation. Red arrow is the spin excitation.

as shown in Fig. 1.11(c). In this case, quantum fluctuation is enhanced because many patterns of singlet pairs are degenerated. There is no magnetic long-range order for such a state, and such state is also called as the 'spin liquid state'. There are two versions for the RVB state: short-range RVB state and long-range RVB state. The short-range RVB state considers only the valence bond between the closest spins, and it has a spin gap. On the other hand, if the singlet bond is formed with a long distance, it is easier to break up the singlet pair, and the excited state is gapless. Such RVB state, which consider the long-range bond, is called the long-range RVB state.

The first excitation of the RVB state can be created by breaking a valence bond, where the elementary excitation is called a spinon. These created two spinons can be separated in a finite distance since the energy cost would be the same with any distance. Hence, it is considered that the spinons are deconfined.

The spins for the RVB state form singlets at the zero-temperature, and the magnetic susceptibility will be zero. The short-range RVB state has no entropy at $T = 0$ due to the gapped excitation, hence, heat capacity will be zero at $T = 0$. For the case of long-range RVB state, which is gapless, the heat capacity is expected to have a T-linear term at the zero-temperature limit because of the residual entropy.

Another spin liquid state, such as the spinon Fermi surface, is also proposed. In the spinon Fermi surface, the spin excitation with $S = 1/2$ has a Fermi surface like an electron. [27]. This state has gapless spinon excitations over the entire Fermi surface, and spin susceptibility is

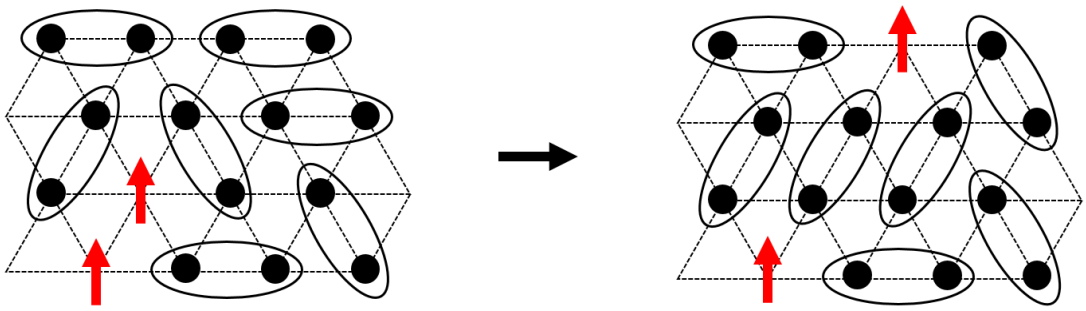

Figure 1.13: Two spin excitation in the RVB state. Red arrow is the spin excitation.

expected to be finite at $T = 0$. [28] And the entropy remains at $T = 0$ because of the gapless spin excitation, therefore heat capacity measurement is expected to have a T-linear term in the zero-temperature limit.

In the next section, the molecular Mott insulators $X[Pd(dmit)_2]_2$ (X = Me_4P, Et_2Me_2P, Me_4Sb, $EtMe_3Sb$, Et_2Me_2Sb and $EtMe_3P$) with triangular lattice will be introduced.

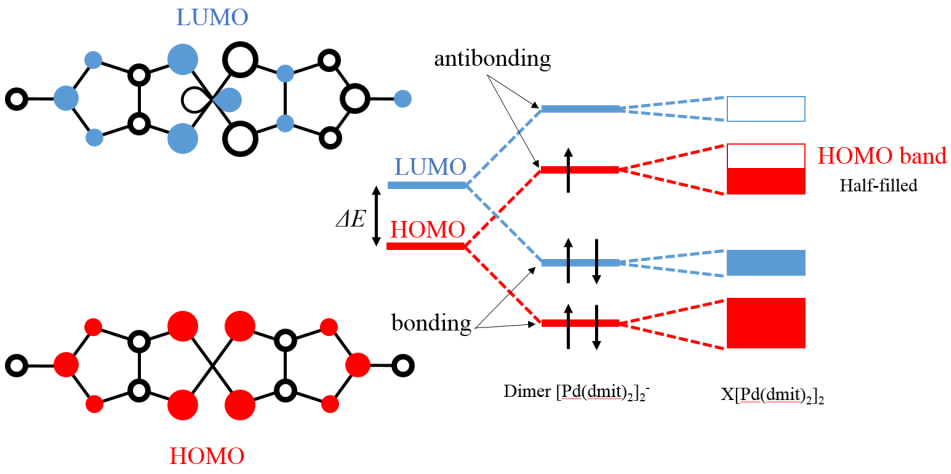

Figure 1.14: HOMO and LUMO of a $Pd(dmit)_2$ dimer and schematic electronic structure for a $Pd(dmit)_2$ dimer unit. ΔE is the energy gap between HOMO and LUMO.

1.3 The molecular-based triangular lattice system $X[Pd(dmit)_2]_2$

The anion radical salts $X[Pd(dmit)_2]_2$ (X is monovalent cation, such as Me_4P, Et_2Me_2P, Me_4Sb, $EtMe_3Sb$, Et_2Me_2Sb and $EtMe_3P$), which have a triangular lattice, show a wide variety of ground states. [16, 29–31]

In $X[Pd(dmit)_2]_2$, the $Pd(dmit)_2$ is an acceptor molecule which becomes stable by accepting an electron from the monovalent cation X. [16, 17] Moreover, $X[Pd(dmit)_2]_2$ has a unique HOMO–LUMO structure due to the central core of the $Pd(dmit)_2$, which is the transition metal ion Pd. The *d*-orbital of the central core metal has a very small overlap with the ligand orbitals in the HOMO due to its symmetry (Fig. 1.14). The absence of the metal-ligand interaction raises the HOMO energy level, and the HOMO-LUMO energy gap ΔE is reduced as shown in Fig. 1.14. [16,17,32] Furthermore, $Pd(dmit)_2$ units are strongly dimerized by Pd-Pd interaction. HOMO and LUMO form bonding and antibonding pairs by the dimerization of $Pd(dmit)_2$ moecules. The strong dimerization provides a large energy difference between the bonding and the antibonding pairs. For the $X[Pd(dmit)_2]_2$ case, energy difference between the bonding and the antibonding pairs is large enough, so that the HOMO-LUMO inversion occurs (Fig. 1.14). [17,29,33] For such a case, the HOMO makes the conduction band. Furthermore, this HOMO band has a half-filled conduction band, and the electron on the $Pd(dmit)_2$ dimer cannot hop to the other dimer due to the strong on-site Coulomb repulsion. Therefore, $X[Pd(dmit)_2]_2$ is a Mott insulator at ambient pressure. [17, 29, 33] Hence, in $X[Pd(dmit)_2]_2$,

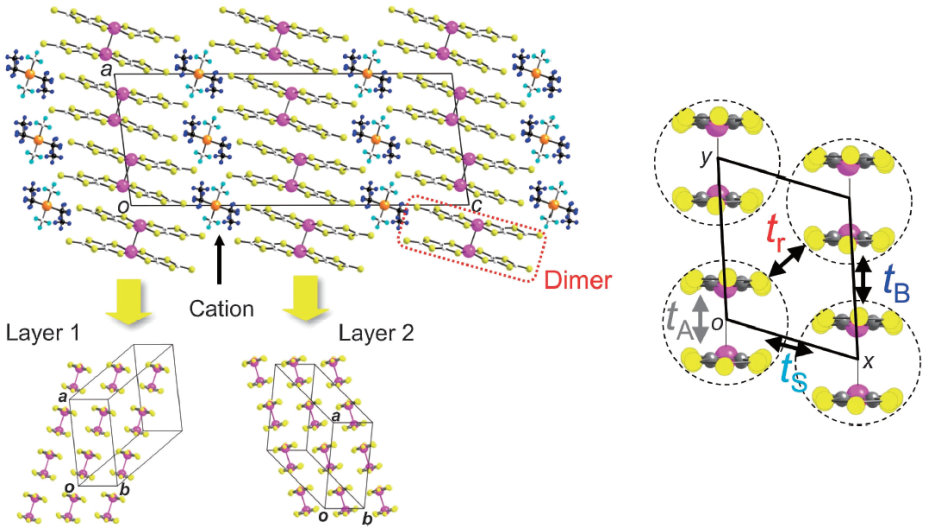

Figure 1.15: The crystal structure of β'-X[Pd(dmit)$_2$]$_2$ (X=Me$_4$P, Et$_2$Me$_2$P, Me$_4$Sb, EtMe$_3$Sb, Et$_2$Me$_2$Sb). The space group of $C2/c$. $t = t_S \sim t_B$ and $t' = t_r$. [16]

an unpaired electron $S = 1/2$ is localized on the Pd(dmit)$_2$ dimer, and the Pd(dmit)$_2$ dimers form a triangular lattice as shown in Fig. 1.15. [16, 17, 29–31] In this system, the anisotropy of the triangular lattice is expressed by the transfer integrals t and t' ratio, t'/t (Fig. 1.15). This anisotropy of the triangular lattice is related to the geometrical frustration. One of the fascinating features in this system is that the geometrical frustration can be controlled by the monovalent cation X. [16, 17, 29–31] Indeed, β'-X[Pd(dmit)$_2$]$_2$ (X = Me$_4$P, Et$_2$Me$_2$P, Me$_4$Sb, EtMe$_3$Sb, Et$_2$Me$_2$Sb) has different ground states depending on the frustration parameter t'/t as shown in Fig. 1.16. The antiferromagnetic ground state is observed for $t'/t < 0.87$, the quantum spin liquid state is observed for $0.87 \leq t'/t < 0.95$, and the charge ordered state is observed for $0.95 \leq t'/t$. [16, 17, 30, 31] β'-X[Pd(dmit)$_2$]$_2$ has the space group of $C2/c$ and a 'solid cross column' structure, where adjacent layers have the cross stacking direction as shown in Fig. 1.15. The unit cell contains two crystallographically equivalent Pd(dmit)$_2$ columns parallel to the $a + b$ and a - b directions as shown as Layer 1 and Layer 2 in Fig. 1.15, respectively. In contrast, EtMe$_3$P[Pd(dmit)$_2$]$_2$ has a 'parallel-column' structure (Fig. 1.17). Although, the Pd(dmit)$_2$ dimers in EtMe$_3$P[Pd(dmit)$_2$]$_2$ also form a triangular lattice with a $t'/t \sim 1$ (regular triangular lattice), it shows a valence bond order (VBS) state due to the 'parallel-column' structure.

The physical properties of β'-X[Pd(dmit)$_2$]$_2$ and EtMe$_3$P[Pd(dmit)$_2$]$_2$ salts will be intro-

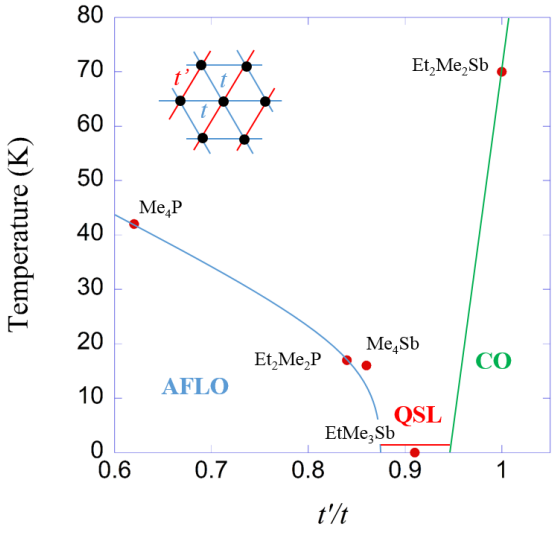

Figure 1.16: The phase diagram of X[Pd(dmit)$_2$]$_2$. t'/t is frustration parameter [16]

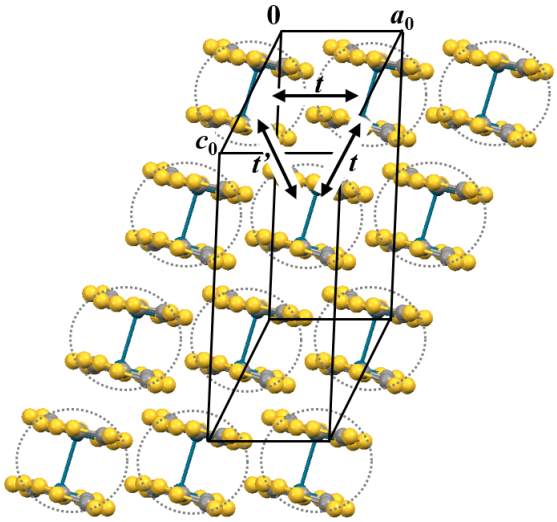

Figure 1.17: The crystal structure of EtMe$_3$P[Pd(dmit)$_2$]$_2$. The space group of $P2_1/m$. $t'/t \sim 1$.

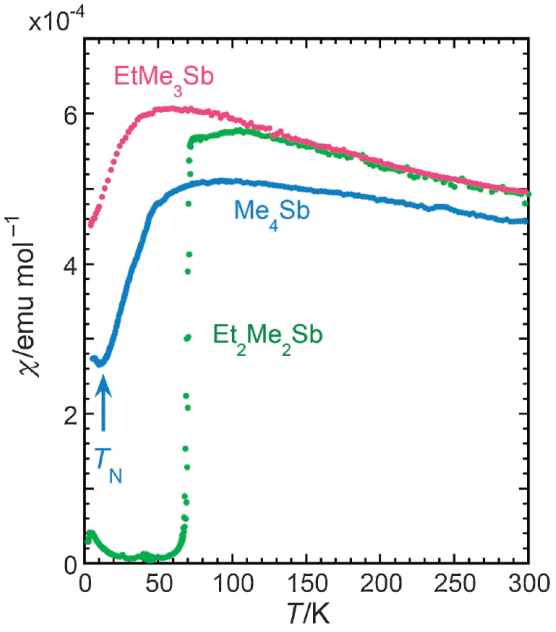

Figure 1.18: Temperature dependence of magnetic susceptibility for β'-X[Pd(dmit)$_2$]$_2$ (X = Me$_4$Sb, EtMe$_3$Sb, Et$_2$Me$_2$Sb). The Curie term is subtracted. [16, 17]

duced in the next sections.

1.3.1 The X = Me$_4$P, Et$_2$Me$_2$P, Me$_4$Sb salts (Antiferromagnetic state)

The anion radical salt β'-X[Pd(dmit)$_2$]$_2$ with the X = Me$_4$P, Et$_2$Me$_2$P, and Me$_4$Sb crystallizes in β'-forms (monoclinic, $C2/c$). These samples are Mott insulators at ambient pressure. The spins with $S = 1/2$ are located on the Pd(dmit)$_2$ dimers, and the Pd(dmit)$_2$ dimer form a triangular lattice.

The magnetic susceptibilities of Me$_4$P, Et$_2$Me$_2$P, Me$_4$Sb salts in the high temperature region are well-described by the model of $S = 1/2$ Heisenberg-type triangular antiferromagnet with the exchange couplings of J = 240-280 K. As shown in Fig. 1.18, the magnetic susceptibility for the X = Me$_4$Sb salt shows a small upturn at low temperature, which is ascribed to the Néel temperature T_N. [16, 34] The respective T_N for each salt is shown in Table 1.1. As shown in Table 1.1, T_N decreases as t'/t increases. Namely, if the sample has more stronger geometrical frustration (t'/t approaches to the unity), antiferromagnetic state appears at lower temperature. These results suggest that the geometrical frustration suppresses the antiferromagnetic state. The antiferromagnetic state is confirmed also from NMR, where typical NMR spectra of the antiferromagnetic state and the characteristic behavior of the

	t'/t	T_N (K)
$Me_4P[Pd(dmit)_2]_2$	0.62	42
$Et_2Me_2P[Pd(dmit)_2]_2$	0.84	17
$Me_4Sb[Pd(dmit)_2]_2$	0.86	16

Table 1.1: t'/t and Néel temperature of Me_4P, Et_2Me_2P, Me_4Sb salts [16, 17, 30, 31]

spin-lattice relaxation rate $1/T_1$ are observed. [35, 36] Among the three samples, the high-field ESR measurement has been performed on Et_2Me_2P salt, where the antiferromagnetic resonance (AFMR) is observed. [37]

1.3.2 The X = $EtMe_3Sb$ salt (Quantum spin liquid state)

The anion radical salt $EtMe_3Sb$ has a unique ground state. Although, the crystal structure is the same as the previous section, the t'/t of $EtMe_3Sb$ salt is 0.91, which is almost a regular triangular lattice. [16,29–31] Because of such almost isotropic triangular lattice, it is considered that the sample has strong geometrical frustration.

The magnetic susceptibility of the X = $EtMe_3Sb$ salt is shown in Fig. 1.18. [16] No magnetic transition occurs for the $EtMe_3Sb$ salt down to 4.5 K. In addition to this, other measurements, such as NMR and μSR, confirm that there is no long-range order down to few tens of mK. Figure 1.19 is ^{13}C NMR results of the $EtMe_3Sb$ salt. [16, 38, 39] This result indicates that there is no long-range order down to 19 mK. It is considered that the ground state is in the quantum spin liquid (QSL) state.

Moreover, Fig. 1.20 is the temperature dependence of the spin-lattice relaxation rate $1/T_1$. The relaxation curve was fitted by the stretched exponential function, 1-$M(t)/M(\infty)$ = exp-$(t/T_1)^\beta$, where $M(t)$ is spin-echo intensity after a time delay t and β is the stretching exponent. The stretching exponent β indicates how homogeneous the system is. When $\beta = 1$, the system is homogeneous, and the β value smaller than unity means that the system is inhomogeneous. The relaxation rate clearly indicates a kink around 1 K. This suggests that the spin state undergoes to an abrupt change at 1 K. Since discontinuous jump is not observed, the change of the spin state is likely to be a crossover. Below 1 K, the $1/T_1$ is proportional to T^2. This is not the nature of a gapless spin liquid state. Thus, the autors in Ref. [40] claim that the lower temperature state has a spin gap.

Heat capacity and thermal conductivity provide information about the low-energy exci-

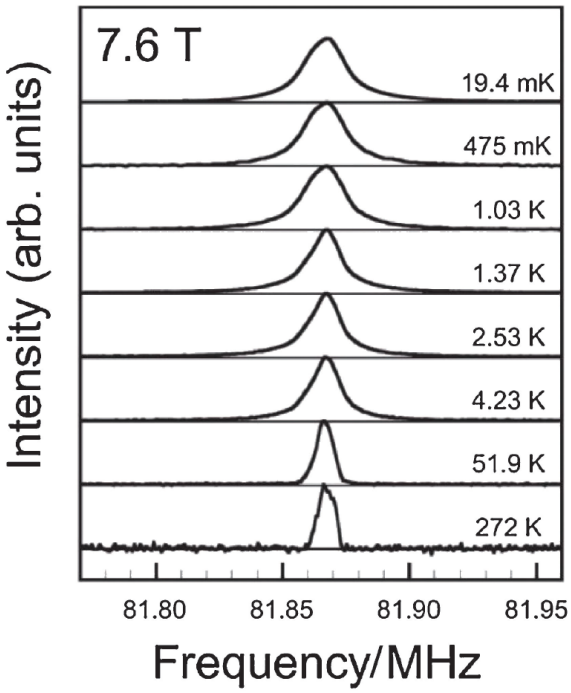

Figure 1.19: ^{13}C NMR for $EtMe_3Sb[Pd(dmit)_2]_2$. [16]

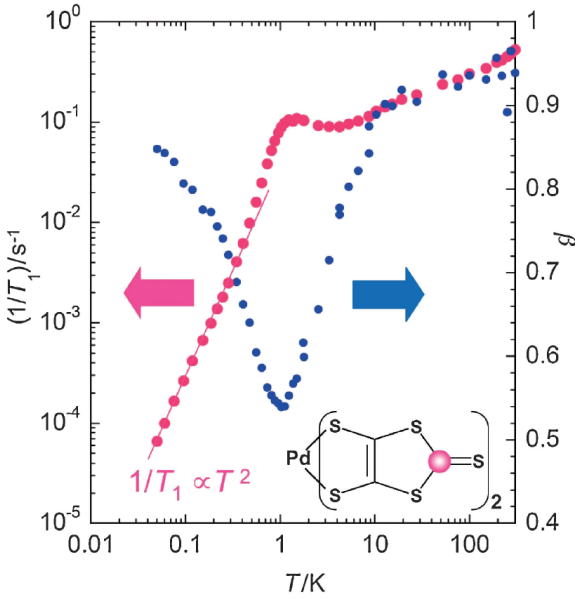

Figure 1.20: Temperature dependence of the ^{13}C nuclear spinlattice relaxation rate $1/T_1$ and stretching exponent β for $EtMe_3Sb[Pd(dmit)_2]_2$. [16]

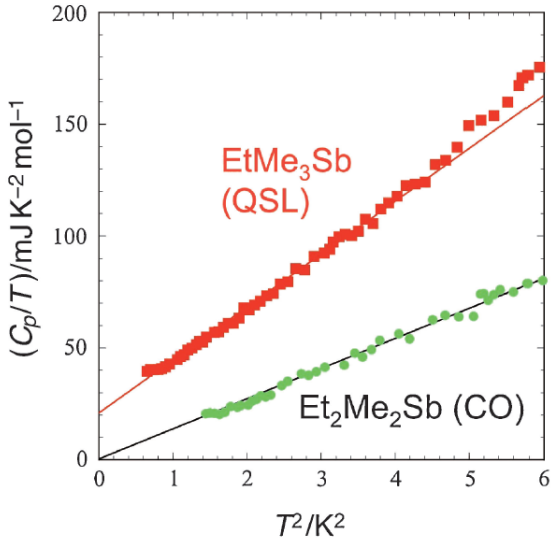

Figure 1.21: Low-temperature heat capacity C_p for $EtMe_3Sb$ and Et_2Me_2Sb salt plotted in C_p/T versus T^2. [16, 18]

tations. In Fig. 1.21, the $EtMe_3Sb$ salt shows a T-linear term in the zero-temperature limit. Such behavior is generally observed for typical metals despite that the $EtMe_3Sb$ salt is a Mott insulator. [18] The finite T-linear term suggests the existence of deconfined spins, and the spin excitation is gapless.

In Fig. 1.22, temperature dependences of the thermal conductivity divided by T for the $EtMe_3Sb$ salt is shown as κ/T vs. T^2. [19] The thermal conductivity data give information on the spin-mediated heat transport. Compared with the CO system, which will be explained in the following section, the $EtMe_3Sb$ salt shows a huge thermal conductivity indicating that spin-mediated contribution is added to the phonon contribution. And thermal conductivity also shows a finite T-linear term, as it was the case of the heat capacity. This implies that the excitation from the ground state is gapless. The heat capacity and the thermal conductivity measurements indicate that the $EtMe_3Sb$ salt is a gapless spin liquid. However, temperature dependence of spin-lattice relaxation rate $1/T_1$ of ^{13}C NMR suggests a gapped spin liquid state. [40]

Therefore, there are strong debates whether the spin liquid state is gapped or gapless.

On the other hand, recently, there has been a report on NMR results for ^1H, ^2D, and ^{121}Sb. [41] This result shows that there is the charge fluctuation, which can prevent magnetic ordering and contribute the spin liquid state, at the lowest temperature. [41] Namely, there is

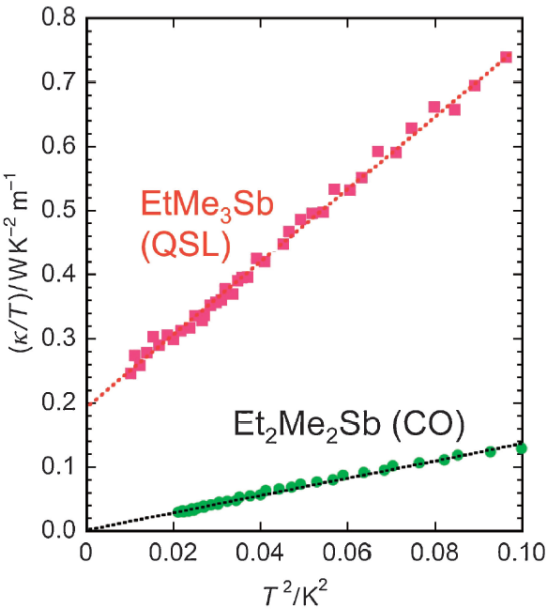

Figure 1.22: Low-temperature thermal conductivity κ for $EtMe_3Sb$ and Et_2Me_2Sb salt plotted in κ/T versus T^2. [16, 19]

possibility of not only the geometrical frustration but also charge fluctuation affect the spin liquid ground state.

Thus, the spin liquid state ground state of this sample is still controversial.

1.3.3 The X = Et_2Me_2Sb salt (Charge-ordered state)

The Et_2Me_2Sb salt has a regular triangular lattice ($t'/t = 1$). Thus, there should be a strong frustration effect. However, Et_2Me_2Sb salt has different ground state with the other previous salts. As shown in Fig. 1.18, Et_2Me_2Sb salt become non-magnetic at 70 K. [16, 42] It is obvious that it has different ground state with the spin liquid state or the antiferromagnetic state. At room temperature, every dimer is crystallographically equivalent with the Pd-Pd distance of 3.137 Å. [43] However, at 10 K, Et_2Me_2Sb salt has two crystallographically independent dimers with Pd-Pd distances of 3.331 Å and 2.924 Å. [43] These dimers are alternately arranged along the b axis as shown in Fig. 1.23. [43] As shown in Fig. 1.24, the short Pd-Pd distance (2.924 Å) enhances the dimerization, and expands the dimerization gap. In contrast, the long Pd-Pd distance (3.331 Å) reduces the dimerization gap. For this reason, one electron of the antibonding HOMO from the shrinked dimer move to the antibonding HOMO of the expanded dimer (Fig. 1.24). [16, 42] Thus, Et_2Me_2Sb has the charge-ordered

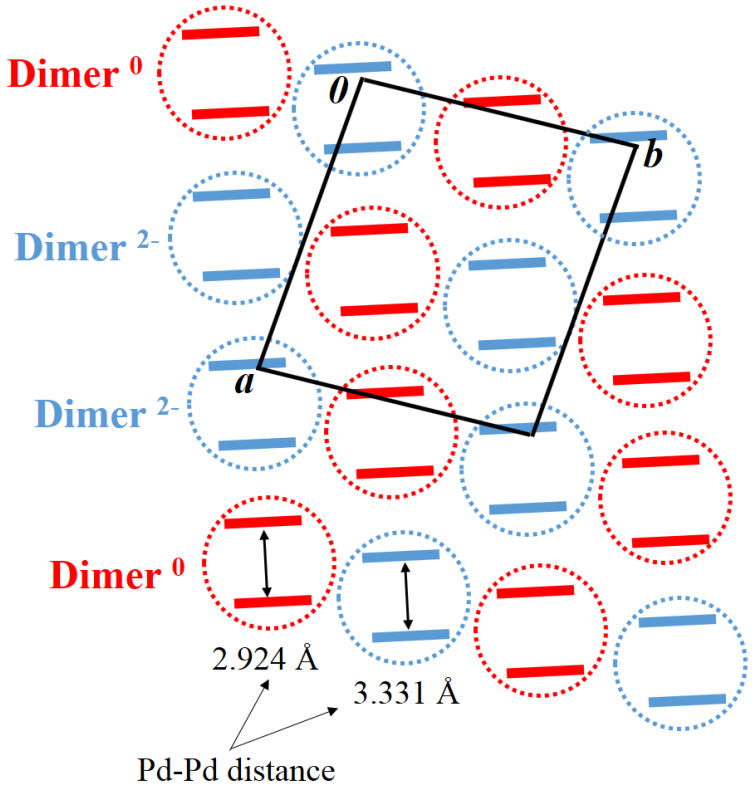

Figure 1.23: Crystal structure of Et_2Me_2Sb salt at 10 K.

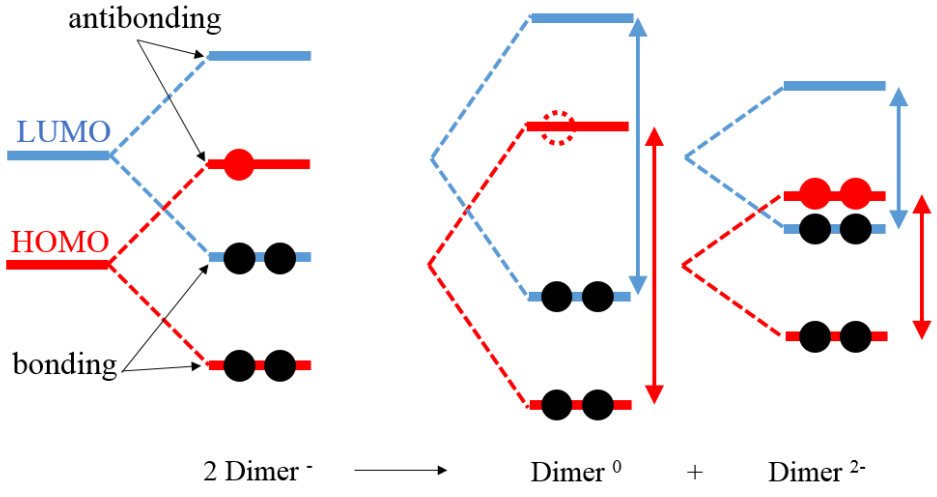

Figure 1.24: Energy scheme for the charge-ordered transition in Et_2Me_2Sb salt.

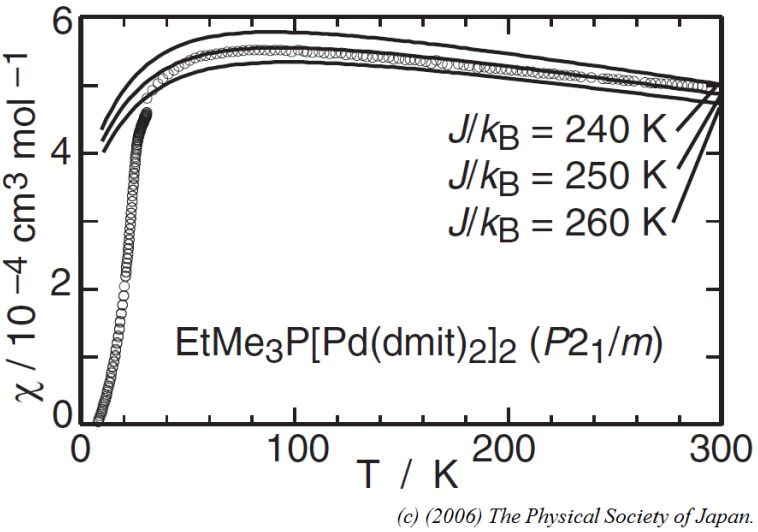

(c) (2006) The Physical Society of Japan.

Figure 1.25: Temperature dependence of the magnetic susceptibility of the $EtMe_3P$ salt. Solid curves are the calculations for the $S = 1/2$ Heisenberg triangular antiferromagnets with the indicated exchange coupling parameters. [45]

(CO) state, where two monovalent dimers turn into the neutral and divalent dimers for the constricted dimer and the expanded dimer, respectively. [16,42] There is no any unpaired spin on the dimer, and the system becomes non-magnetic.

1.3.4 The X = $EtMe_3P$ salt (The Valence Bond Solid state)

The anion radical salt $EtMe_3P[Pd(dmit)_2]_2$ crystallizes in monoclinic (space group of $P2_1/m$), triclinic (space group of $P\bar{1}$), and β'-forms (monoclinic, space group of $C2/c$). Here, the monoclinic ($P2_1/m$) is the main product. [16,44] In this thesis, the monoclinic ($P2_1/m$) sample will be introduced. As described in the previous section, $EtMe_3P[Pd(dmit)_2]_2$ is also a Mott insulator at ambient pressure. The spins also form a triangular lattice with a $t'/t \sim 1$(regular triangular lattice).

The magnetic susceptibility of $EtMe_3P[Pd(dmit)_2]_2$ in the high temperature region is well-described by the model of $S = 1/2$ Heisenberg-type isotropic triangular lattice with exchange couplings of $J = 250$ K (Fig. 1.25). [45] In the low temperature region, a rapid decrease of the magnetic susceptibility towards $\chi \sim 0$ accompanied with a structural change is observed at 25 K. Below 25 K, double periodicity along the c - a direction (the stacking direction) is confirmed by the X-ray diffraction as shown in Fig. 1.26. All the dimers are crystallographically equivalent, but no longer centrosymmetric due to the alternating interdimer interactions. The

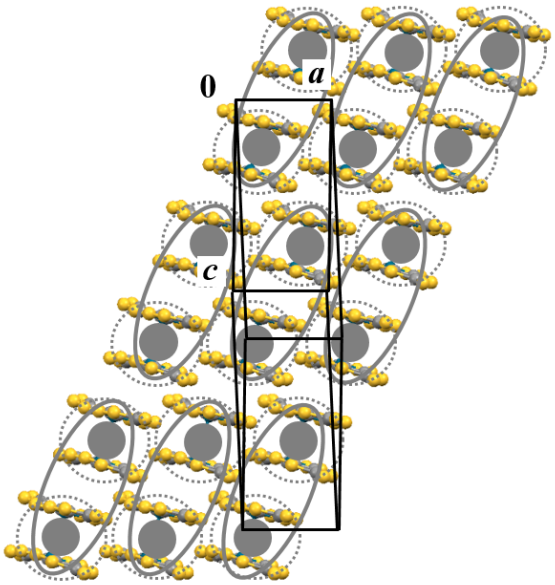

Figure 1.26: The crystal structure of $EtMe_3P[Pd(dmit)_2]_2$ ($P2_1/m$ form) at at 10 K. Below $T_{VBS} = 25$ K, double periodicity is observed along the stacking (c - a) direction. The grey solid circles and open ovals represent the $S = 1/2$ on the dimers and the valence bonds, respectively.

interdimer spacing along the stacking direction shows two-fold alternation of 3.67 and 3.85 Å, whereas the interdimer spacing is uniform above T_{VBS} (e.g. 3.82 Å at 28 K). In analogy with the spin-Peierls transition observed in the one-dimensional (1D) spin system, this structural change induces a pairing of the nearest neighbor dimers forming $S = 0$ valence bond as schematically shown as grey oval in Fig. 1.26. Hence, it is considered that the structural change at 25 K breaks the translational symmetry of the triangular lattice, and the system undergoes a valence bond solid (VBS) state that has a non-magnetic singlet ground state. The VBS state below 25 K is also confirmed from recent NMR and thermal expansion measurements, where a rapid decrease of spin lattice relaxation rate $1/T_1$ and distinct anomaly is observed in the thermal expansion coefficients. [46, 47]

The spin-gap is estimated by Tamura *et al.* The energy gap between the singlet ground state and triplet excited state, to be about $\Delta E = 40$ K from the magnetic susceptibility measurement. [45] They used a general formula for obtaining the spin-gap, $\chi(\mathrm{T}) \propto \exp(\Delta E/k_B T)$ for $k_B T \ll \Delta E$. The temperature range of the fitting, however, is very narrow (from 7 to 15 K) and the result is very sensitive to the subtractions of the Curie component from impurities and diamagnetism. [45] Hence, the obtained spin-gap might not be accurate. Although

Ohta *et al.* also estimated $\Delta E = 40$ K by ESR measurement, they argued a possibility of the contamination of another crystal form with the space group of $P\bar{1}$ in their sample. [48] Hence, the reinvestigation of the spin-gap in this system is highly desired.

1.4 Motivations of this study

The anion radical salt β'-X[Pd(dmit)$_2$]$_2$ show a wide variety of ground states, such as antiferromagnetic state, spin liquid state, and charge ordered state, depending on the geometrical frustration. This feature is considered to be an advantage in studying the effect of frustration on the ground state. Therefore, as introduced in the previous section, β'-X[Pd(dmit)$_2$]$_2$ salts have been investigated through various measurements, especially macroscopic measurements such as thermal and static magnetic susceptibility measurements. However, not many ESR measurements, which are microscopic measurement that directly probe the electron, are reported for this interesting system with various ground states.

Moreover, there are some open questions in this system, which need to be solved.

First, in the case of the X = EtMe$_3$Sb salt, there are strong debates whether the spin liquid state is gapped or gapless.

Second, The spin liquid state appears in $0.87 \leq t'/t < 0.95$ region in β'-X[Pd(dmit)$_2$]$_2$ system. Although it is expected that the spin liquid state appears for the regular triangular lattice ($t'/t = 1$), which is mostly frustrated, the charged ordered state appears in Et$_2$Me$_2$Sb[Pd(dmit)$_2$]$_2$ system, which is $t'/t = 1$.

Through the ESR measurements, the microscopic information of the electron spins, such as the ground states, the spin dynamics, or the magnetic excitation can be studied. Moreover, intrinsic spin signal can be distinguished from extrinsic signal by the g-value or linewidth. Therefore, systematic ESR studies which cover various ground states of β'-X[Pd(dmit)$_2$]$_2$ salts need to be performed.

In particular, the spin excitation of EtMe$_3$Sb salt (the spin liquid state) is not perfectly understood, and the amount of elementary excitation of the spin liquid state has not been studied yet. The spin counting method using ESR measurement is a powerful tool to obtain the absolute amount of spins. Hence, the amount of spin excitation can be carified.

Meanwhile, the first VBS material EtMe$_3$P[Pd(dmit)$_2$]$_2$ was found in X[Pd(dmit)$_2$]$_2$ system. This VBS material is expected to have some exotic spin excitations, which has not been clarified yet. Since ESR is a useful tool to investigate the spin excitation, ESR studies of EtMe$_3$P[Pd(dmit)$_2$]$_2$ are performed. In addition to this, the reinvestigation of the spin-gap from previous measurements, is also performed.

In this thesis, the systematic study of the X[Pd(dmit)$_2$]$_2$ system, which have triangular

lattice, is presented. The ground states, spin dynamics, and the spin excitations of this system are discussed.

Cation X	a_0 (Å)	b_0 (Å)	c_0 (Å)	β_0 (°)	t'/t
Me_4P	14.379	6.3539	36.496	98.070	0.62
Et_2Me_2P	14.473	6.3918	37.859	96.009	0.84
Me_4Sb	14.325	6.403	36.893	97.543	0.86
$EtMe_3Sb$	14.503	6.3989	37.244	97.352	0.91
Et_2Me_2Sb	14.632	6.420	37.570	97.54	1
Et_2Me_3P	6.3962	36.6911	7.9290	114.302	1

Table 1.2: Lattice and frustration parameters of X[Pd(dmit)$_2$]$_2$ at room temperature. [16, 17, 30, 31, 43, 44]

Cation X	a (Å)	b (Å)	c (Å)	β (°)
Et_2Me_2Sb	14.5400	12.6660	37.230	98.119
Et_2Me_3P	6.3270	36.6911	14.2620	90.552

Table 1.3: Lattice parameters of X[Pd(dmit)$_2$]$_2$ at 10 K. [43, 44]

1.5 Experimental methods

1.5.1 The sample information

Single crystals of X[Pd(dmit)$_2$]$_2$ (X = Me_4P, Et_2Me_2P, Me_4Sb, $EtMe_3Sb$, Et_2Me_2Sb and $EtMe_3P$) were obtained by air oxidation of X_2[Pd(dmit)$_2$]$_2$ in acetone containing acetic acid at 5–10 °C. [30, 44] The β'-type (space group $C2/c$) crystals (X = Me_4P, Et_2Me_2P, Me_4Sb, $EtMe_3Sb$, Et_2Me_2Sb) were obtained as a single phase, with the exception of the $EtMe_3P$[Pd(dmit)$_2$]$_2$. $EtMe_3P$[Pd(dmit)$_2$]$_2$ contain two crystal forms with the space groups of $P2_1/m$ and $P\bar{1}$. Therefore, the crystals were checked one by one with X-ray diffraction method, and picked up single crystals with the $P2_1/m$ symmetry only. Table. 1.2 shows the lattice and frustration parameters of X[Pd(dmit)$_2$]$_2$ at room temperature.

β'-X[Pd(dmit)$_2$]$_2$ has the 'solid cross column' structure, and $EtMe_3P$[Pd(dmit)$_2$]$_2$ has a 'parallel-column' structure, which are already introduced in section 1.3.

On the other hand, lattice parameters of Et_2Me_2Sb[Pd(dmit)$_2$]$_2$ and $EtMe_3P$[Pd(dmit)$_2$]$_2$ are changed at low temperature. The details are already introduced in Section 1.3.3 and 1.3.4. Table. 1.3 shows the lattice parameters of Et_2Me_2Sb[Pd(dmit)$_2$]$_2$ and $EtMe_3P$[Pd(dmit)$_2$]$_2$ at 10 K.

The relations of the unit cell vectors of $EtMe_3P$[Pd(dmit)$_2$]$_2$ are $a = a_0$, $b = b_0$, $c = 2c_0 + a_0$.

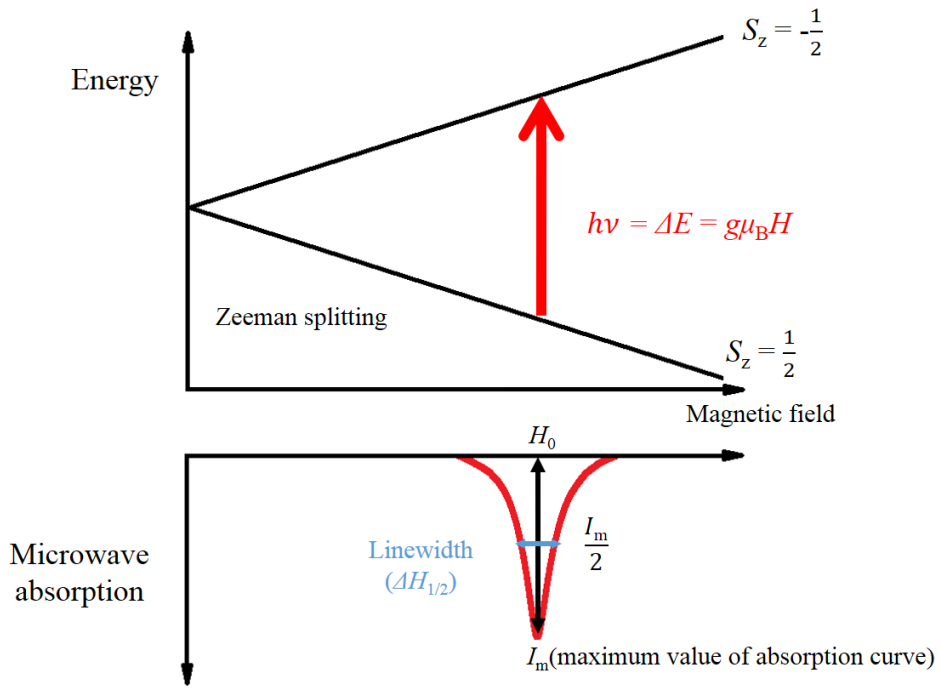

Figure 1.27: The principle of ESR

1.5.2 Electron Spin Resonance

The electron spin resonance measurement is a microscopic measurement that directly probe the unpaired electron. When the external magnetic field is applied to an electron with $S = 1/2$, the Zeeman splitting occurs as shown in Fig. 1.27. When the frequency of the microwave matches with the zeeman splitting, the microwave is absorbed and transition from low energy to high energy levels occurs. The ESR resonance condition is $h\nu = g\mu_B H_0$, where ν is the used microwave and H_0 is the resonance field. The microwave absorption versus the magnetic field is shown in Fig. 1.27. From this microwave absorption line, the resonance field H_0, the linewidth $\Delta H_{1/2}$ and the integrated intensity can be obtained.

The g-value is obtained from the resonance field using the resonance condition mentioned above. The microscopic information surrounding the electron can be obtained from the angular dependence of the g-value since the g-anisotropy reflects the symmetry of the ligand field or the internal field.

The ESR linewidth is related to spin relaxation time. After the ESR transition, the spin system tries to return from the thermal non-equilibrium state to the thermal equilibrium state

. [49] This is called the relaxation process, and the time it takes for the relaxation is called as the relaxation time. There are two types of the relaxation time; one the spin-lattice relaxation time T_1, and the other the spin-spin relaxation time T_2. There is generally a relationship of $T_2 \leqq T_1$ between the T_1 and T_2. The contribution of the spin-lattice relaxtion time to linewidth can be expressed as

$$\Delta H_{1/2}(T_1) = \frac{h}{g\mu_B}\frac{1}{2T_1} = \frac{\pi}{\gamma T_1} \tag{1.2}$$

and the contribution of the spin-spin relaxtion time to linewidth can be expressed as

$$\Delta H_{1/2}(T_2) = \frac{h}{g\mu_B}\frac{1}{T_2} = \frac{2\pi}{\gamma T_2} \tag{1.3}$$

where g is g-value, h is Planck constant, μ_B is Bohr magneton and γ is gyromagnetic ratio. T_1 and T_2 are generally combined in the ESR transition, and can be expressed as a total relaxation time T,

$$\frac{1}{T} = \frac{1}{2T_1} + \frac{1}{T_2} \tag{1.4}$$

Since $T_2 \leqq T_1$, many cases are $1/T \sim 1/T_2$. When only dipole-dipole interaction is considered, the linewidth can be expressed as

$$\begin{aligned} H_d &= \frac{2.35}{g\mu_B}\sqrt{\frac{1}{3}S(S+1)}\sqrt{\sum_j B_{\mathrm{ij}}^2} \\ B_{\mathrm{ij}} &= \frac{\mu_0}{4\pi}\frac{3}{2}g^2\mu_B^2\frac{3cos^2\theta_{\mathrm{ij}}-1}{r_{\mathrm{ij}}^3} \end{aligned} \tag{1.5}$$

where θ_{ij} is the angle between by the direction of the j spin viewed from the i spin and the direction of magnetic field. And r_{ij} is the distance between i spin and j spin. When there is finite exchange interaction, the linewidth narrowing effect occurs, and the ESR linewidth can be expressed as

$$\Delta H_{1/2} \propto \frac{H_d^2}{H_e} \tag{1.6}$$

where H_d is the linewidth obtained from the magnetic dipole interaction, Eq. 1.5, and H_e is the exchange field. Equation 1.6 suggests that the linewidth for magnetic dipole interaction (H_d) narrows with H_d/H_e. This is known as exchange narrowing. [49] If the spin moves, the same effect as the effect of the exchange narrowing appears. This is known as a motional

narrowing.

The integrated intensity of ESR can be obtained from the area of the ESR's absorption line. The integrated intensity of ESR signal is propotional to the spin susceptibility. Therefore, a various information can be obtained through the ESR measurement.

1.5.3 Sample setup for X-band ESR

The studied frequency range was 9 $\sim$ 10 GHz for X-band ESR system (JEOL, JES-RE3X). In this X-band ESR system, the magnetic field modulation technique is used for the high sensitive measurement. As shown in Fig. 1.28, if the AC magnetic field is applied with the static magnetic field H, a spectrum, which is proportional to the absorption line slope can be obtained. In general, the ESR absorption curve is expressed by a Lorentzian lineshape equation

$$L(H) = \frac{I_m}{1 + [(H - H_0)/(\Delta H_{1/2}/2)]^2} \tag{1.7}$$

where, I_m is maximum value of absorption curve, H_0 is resonance field, $\Delta H_{1/2}$ is the linewidth. [49] But, in the case of using the magnetic field modulation technique, the ESR absorption curve is expressed first-derivative of Lorentzian lineshape equation

$$L'(H) = \frac{16 I'_m (H - H_0)/(\Delta H_{\rm pp}/2)}{[3 + \{(H - H_0)/(\Delta H_{\rm pp}/2)\}^2]^2} \tag{1.8}$$

where, I'_m is peak-to-peak intensity, H_0 is resonance field, $\Delta H_{\rm pp}$ is the peak-to-peak linewidth. [49]

For the X-band ESR measurements, the magnetic field was swept between 0.27 and 0.35 T. The sample was cooled using a liquid-helium flow cryostat for X-band ESR (Oxford Instruments). The sample was mounted on a quartz rod as shown in Fig. 1.29, and inserted in the cylindrical cavity with TE_{011} mode.

The magnetic field was applied horizontally to the quartz rod, and angular dependent ESR measurement was performed by rotating the quartz rod. The error range was within few degrees.

For the temperature dependent ESR measurement, many single crystals were stacked and aligned along perpendicular to the crystal plane c-axis (β'-X[Pd(dmit)$_2$]$_2$) and the b-axis ($EtMe_3P$[Pd(dmit)$_2$]$_2$) for increasing the ESR's integrated intensity in the high temperature

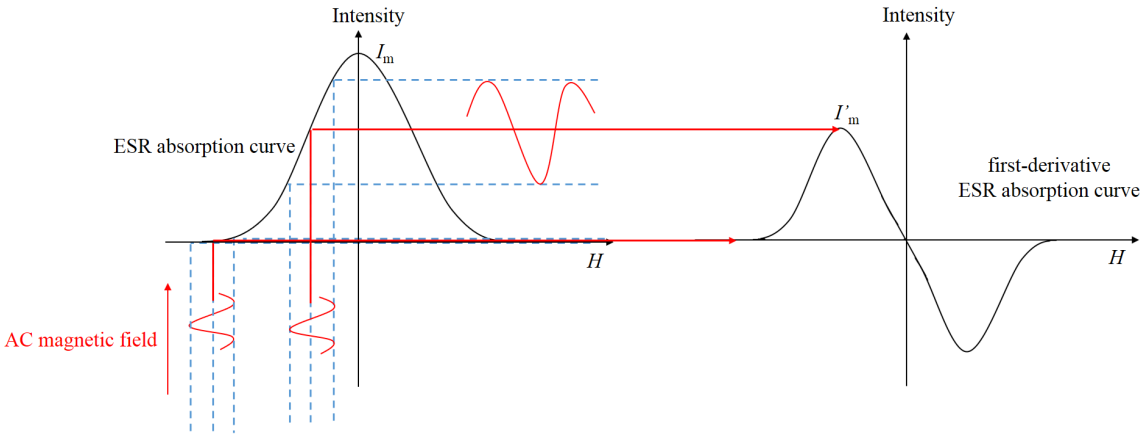

Figure 1.28: The magnetic field modulation technique.

region. Hence, the measurement was performed along $B//c$ (for β'-X[Pd(dmit)$_2$]$_2$) and along $B//b$ (for EtMe$_3$P[Pd(dmit)$_2$]$_2$) only (Fig. 1.29(a)).

One single crystal of β'-X[Pd(dmit)$_2$]$_2$ and EtMe$_3$P[Pd(dmit)$_2$]$_2$ were used for the angular dependent ESR measurement, and the crystal axes of the single crystal were checked beforehand by X-ray diffraction method. The β'-X[Pd(dmit)$_2$]$_2$ and EtMe$_3$P[Pd(dmit)$_2$]$_2$ were mounted so that magnetic field was applied parallel to the ab-plane and the ac-plane, respectively. In the case of EtMe$_3$P[Pd(dmit)$_2$]$_2$ the angle between the magnetic field direction and the c-axis (θ) was determined in the low temperature phase (Fig. 1.29(b)). In this study, θ = 0° and 90° corresponds to the magnetic field direction (approximately) along c-axis and -a-axis, respectively (Fig. 1.30).

1.5.4 Sample setup for V- and W-band ESR

The V- and W-band ESR studies were performed using a millimeter vector network analyzer (AB millimetre, MVNA-8-350-1-2). The studied frequency range was 50 $\sim$ 75 and 75 $\sim$ 100 GHz for V- and W-band, respectively. For the V- and W-band ESR measurements, the sample was directly mounted on the end-plate of the cylindrical cavity with TE$_{011}$ mode.

The magnetic field was applied vertically to bottom plane of the cavity. For the temperature dependent V- and W-band ESR measurement, many single crystals were stacked and aligned along perpendicular to the crystal plane c-axis (β'-X[Pd(dmit)$_2$]$_2$) and the b-axis (EtMe$_3$P[Pd(dmit)$_2$]$_2$) for increasing the ESR's integrated intensity. Because sig-

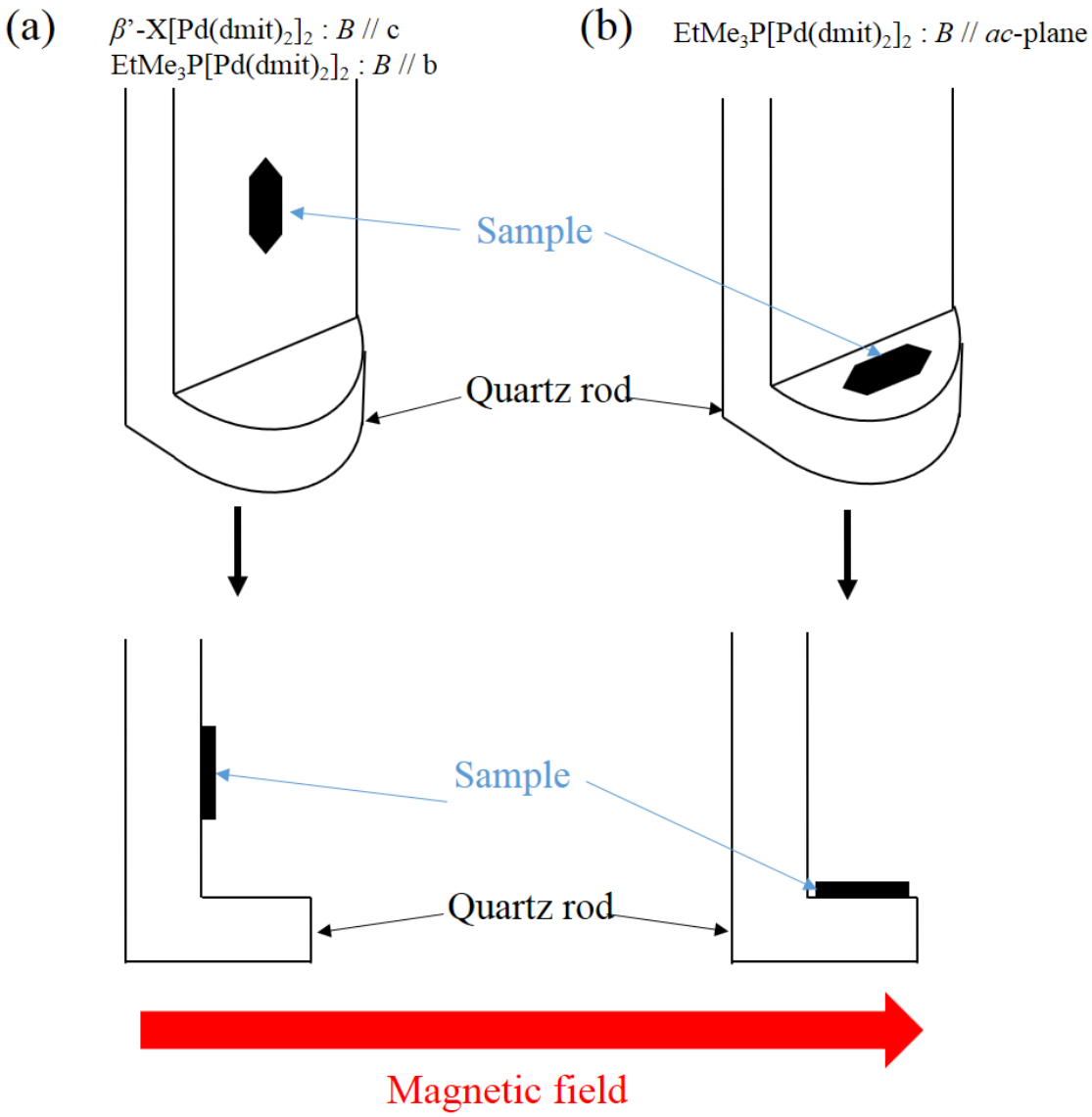

Figure 1.29: Drawings of the sample mounted on the quartz rod for X-band ESR.

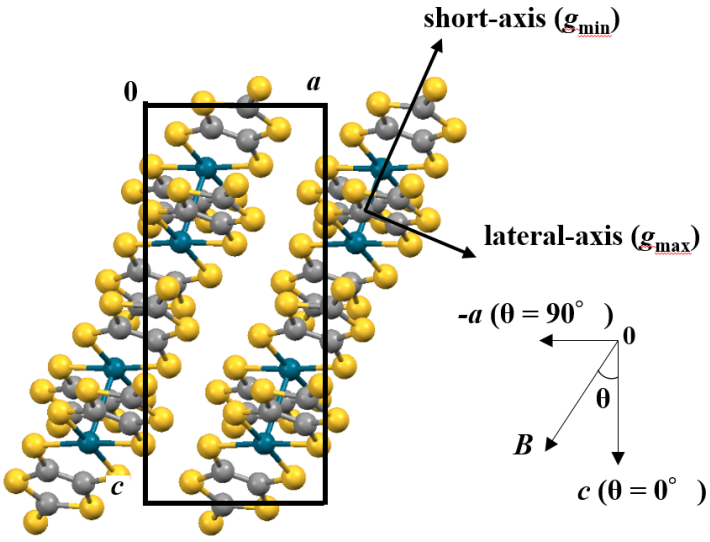

Figure 1.30: The crystal structure viewed from the b-axis. θ is the angle between the magnetic field and the c-axis below T_{VBS}.

nal is very weak. The measurement was performed for $B//c$ (β'-X[Pd(dmit)$_2$]$_2$) and $B//b$ (EtMe$_3$P[Pd(dmit)$_2$]$_2$) only, because the sample can not be rotated in cavity (Fig. 1.29(a)).

1.5.5 Spin counting method

The spin counting method was performed to obtain the amount of remaining spin in the ground state. For the spin counting method, standard sample $CuSO_4 \cdot 5H_2O$ and the sample for spin counting are measured at the same time using the X-band ESR. Figure 1.31 is the drawings of the samples mounted on the quartz rod for the spin counting method. The $CuSO_4 \cdot 5H_2O$ has the g-value of about $2.12 \sim 2.24$ depending on the crystal orientation, so the direction of $CuSO_4 \cdot 5H_2O$ needs to be adjusted so that it does not to overlap with the sample signal. The $CuSO_4 \cdot 5H_2O$ was shredded into pieces of few micrograms since it has huge signal than the sample. And multiple samples were mounted to obtain a larger signal because the sample signal is very small. The absolute spin number of the sample under investigation can be obtained by comparing the integrated intensity of the standard sample.

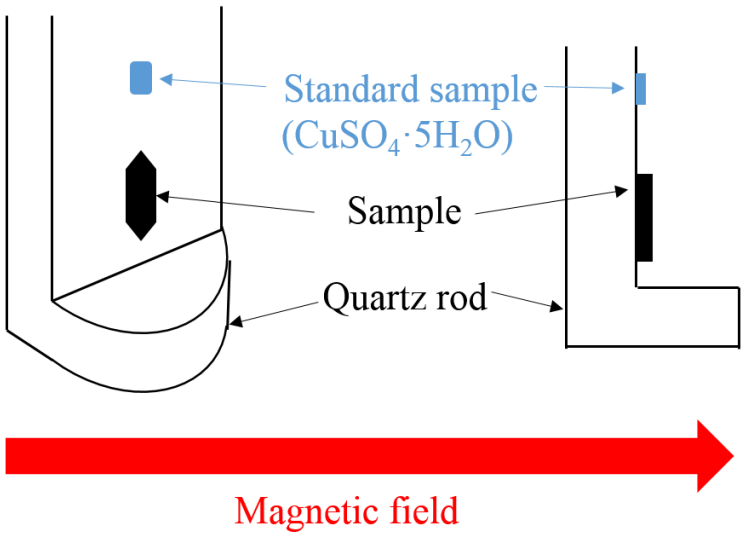

Figure 1.31: Drawings of the sample mounted on the quartz rod for the spin counting method using X-band ESR.

Chapter 2

Results and Discussions

2.1 The X = Me_4P, Et_2Me_2P, Me_4Sb, $EtMe_3Sb$, Et_2Me_2Sb salts

2.1.1 The ESR measurement results

First, ESR measurement results of the X=Me_4P salt, which has the most small frustration parameter $t'/t = 0.62$ in the (β'-X[Pd(dmit)$_2$]$_2$ system, are introduced. As mentioned in section 1.3.1, the X = Me_4P salt is considered to have the antiferromagnetic ground state. Figures 2.1(a) and (b) are the temperature dependence of the integrated intensity, the g-value and the linewidth. The temperature dependence measurements have been performed with the magnetic field applied parallel to the c-axis (i.e. perpendicular to the triangular lattice). As described in section 1.5.2, the integrated intensity of the ESR signal is proportional to the spin susceptibility. The ESR signal of the X = Me_4P salt disappears around the Néel temperature ($T_N = 42$ K) as shown in Fig. 2.2 and Fig. 2.1(a). As shown in Fig. 2.1(b), the g-value and the linewidth decrease by decreasing the temperature, and a steep increase are both observed just above T_N. This steep increase of the g-value and linewidth above T_N is a typical precursor of antiferromagnetic long-range order, and is due to the development of antiferromagnetic correlation. Hence, the observed ESR signal can be attributed to an electron paramagnetic resonance (EPR), and EPR signal is lost below T_N since the ground state turns into an antiferromagnetic ground state. According to these results, the X = Me_4P salt learly shows a typical behavior of the antiferromagnetic state.

Next, Figs. 2.3(a) and (b) are the temperature dependence of the integrated intensity, the g-value and the linewidth for the X = $EtMe_3Sb$ salt ($t'/t = 0.91$), which is the candidate

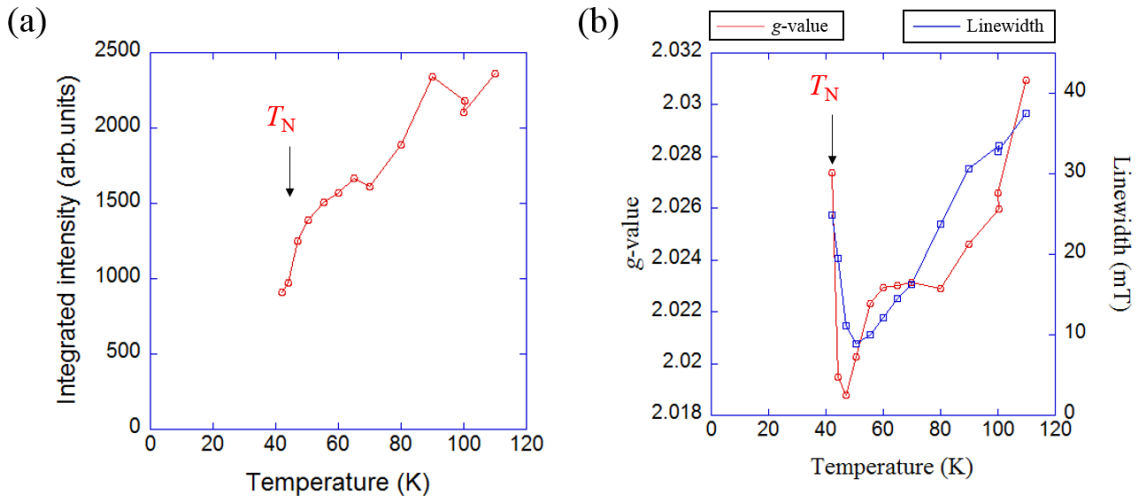

Figure 2.1: The temperature dependence of (a) the ESR integrated intensity, (b) the g-value and the linewidth for the X = Me_4P salt ($B//c$). The g-value and the linewidth is presented by red open circles and blue open squares, respectively.

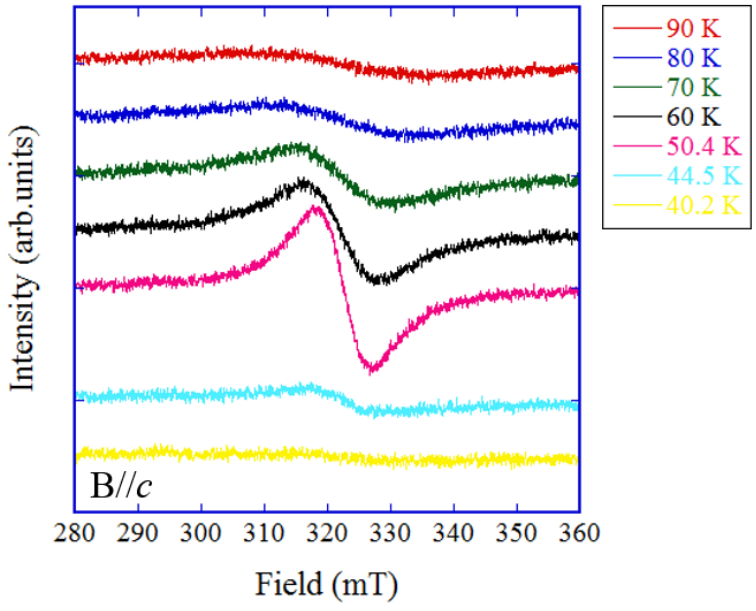

Figure 2.2: The ESR spectra of the temperature dependence measurements for Me_4P salt ($B//c$).

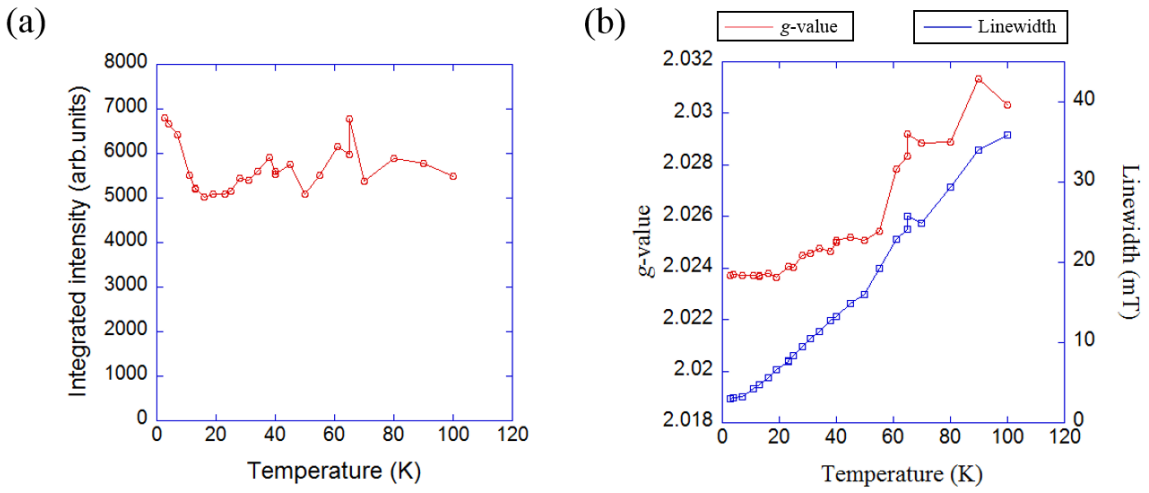

Figure 2.3: The temperature dependence of (a) the integrated intensity, (b) the g-value and the linewidth for $EtMe_3Sb$ salt ($B//c$). The g-value and the linewidth is presented by red open circles and blue open squares, respectively.

material for the spin liquid ground state (section 1.3.2). The temperature dependence measurements have also been performed for $B//c$-axis. As shown in Fig. 2.3(a), the ESR signal remains down to the lowest temperature. And the g-value becomes temperature-independent below 20 K as shown in Fig. 2.3(b). Moreover, the linewidth narrowing with the linear temperature dependence below 40 K is noticed from Fig. 2.3(b). From the results, the antiferromagnetic transition does not occur for the X = $EtMe_3Sb$ salt because no rapid decrease of the integrated intensity nor steep increase in the g-value and the linewidth are observed. And it can be confirmed that spins remain at low temperature from the temperature dependence of integrated intensity. So, in order to investigate the origin of this remaining spin, the angular dependent measurements were performed by applying a magnetic field parallel to the triangular lattice. The ESR spectra of the angular dependence measurements is shown in Fig. 2.4. [50]. The angular dependence measurements have been performed for $B//ac$-plane. From the ESR spectra, two ESR signals are observed. The existence of two signals reflects the solid cross column structure with different Layer1 and Layer2 direction as shown in Fig. 2.5 (right). The angular dependence of the g-value and the linewidth for $B//ac$-plane is shown in Fig. 2.5 (left). [50] Here, the g-value and the linewidth are presented by the red open circles and the blue open squares. The angular dependence of the g-value is well-fitted with the typical anisotropy of the g-value, $g_{\text{eff}} = \sqrt{(g_{\text{max}}cos(\theta - \theta_{\text{max}}))^2 + (g_{\text{min}}sin(\theta - \theta_{\text{max}}))^2}$, where g_{max} is

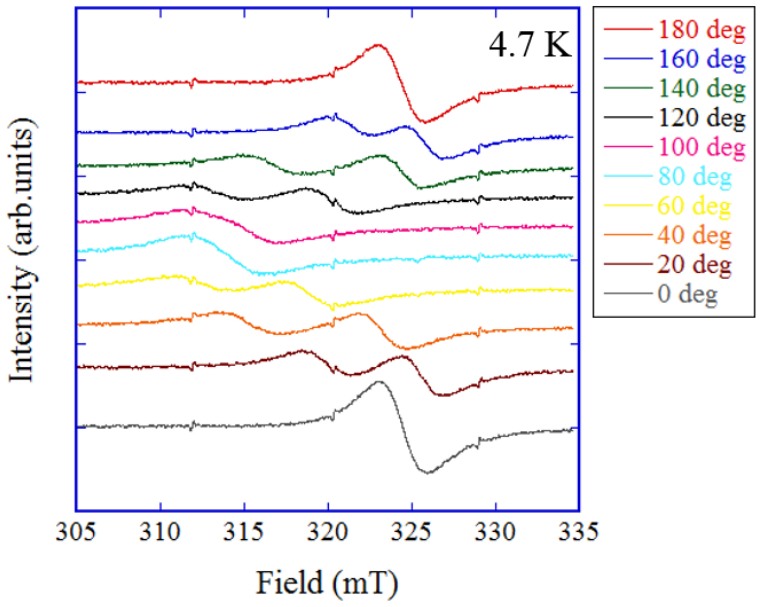

Figure 2.4: The ESR spectra of the angular dependence for $EtMe_3Sb$ salt ($B//ab$-plane). [50]

the maximum g-value, g_{min} is the minimum g-value and θ_{max} is the degree of maximum g-value. In general, the linewidth obeys with the empirical angular dependence, $1 + \cos^2(\theta - \theta_{max})$, which is related to the magnetic anisotropy. However, the angular dependence of the linewidth of the X = $EtMe_3Sb$ salt does not obey with the empirical angular dependence and the enhancement of the linewidth is observed when the field is applied along the diagonal direction. This means that there is additional contribution in the angular dependence of the linewidth. [50]

Next, Fig. 2.6(a) is the ESR spectra for the X = Et_2Me_2Sb salt ($t'/t = 1$), which is believed to have the charged ordered ground state (section 1.3.3). The temperature dependence measurements have been performed for $B//c$-axis. The ESR signal is very broad and weak at high temperature, hence, it is difficult to obtain the linewidth accurately. In this ESR spectra, the ESR signal shows an asymmetric lineshape, which cannot be fitted with Lorentzian lineshape. So, in order to investigate the asymmetric lineshape, the angular dependence measurements have been performed for $B//ab$-plane. Figure 2.6(b) is the ESR spectra of the angular dependence measurements for the X = Et_2Me_2Sb salt. Two signals are observed from the ESR spectra. It reflects the solid cross column structure, where the $Pd(dmit)_2$ dimers are packed in a different direction in Layer1 and Layer2 (see Fig. 1.15). So, it can be considered

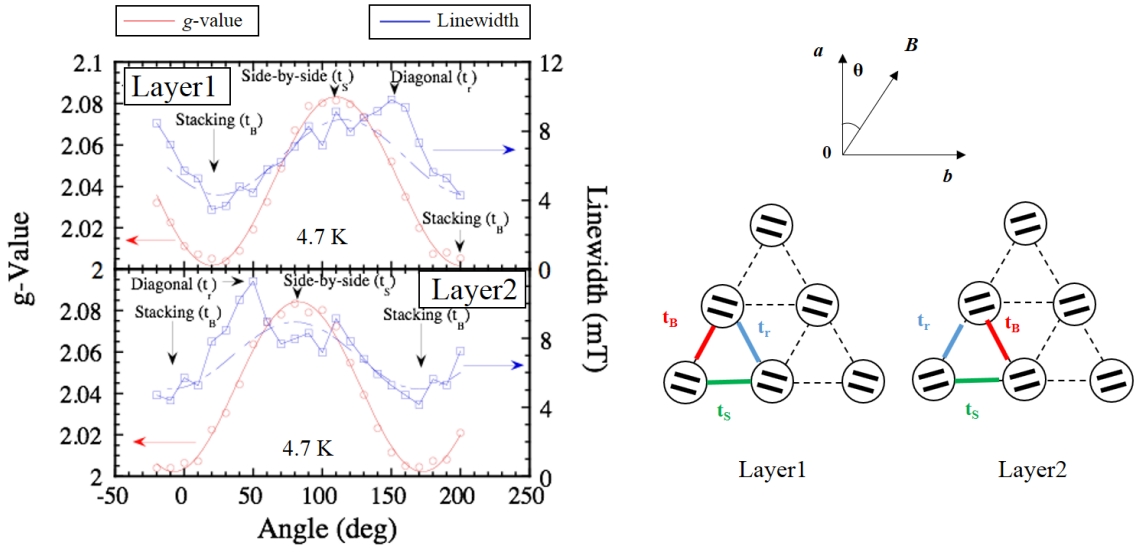

Figure 2.5: The angular dependence of the g-value and the linewidth for $EtMe_3Sb$ salt ($B//ab$-plane). The red solid and dashed curve are the fitting curves for the g-value and linewidth, respectively. (see text) [50]

that the origin of the asymmetric lineshape observed for the temperature dependence measurement is due to two ESR signals. Hence, the asymmetric ESR spectra can be fitted using a double Lorentzian function, which is the sum of two different Lorentzian lineshapes. Figures 2.7(a) and (b) are the temperature dependence of integrated intensity, the g-value and the linewidth. The integrated intensity rapidly decreases around the transition temperature $T_{CO} = 70$ K, but not to be zero as shown in Fig. 2.7(a). The existence of two signals below T_{CO} reflects the Layer1 and Layer2. The g-value and the linewidth decrease above T_{CO}, and become temperature-independent below T_{CO} as shown in Fig. 2.7(b). The observations of temperature-independent g-value and linewidth suggest there is no interaction between the spins. Figure 2.8 is the angular dependence of g-value and linewidth for the X = Et_2Me_2Sb salt at 4.2 K. From the results, angular dependence of the g-value is well-fitted the typical anisotropy of the g-value, and angular dependence of the linewidth is well-fitted the typical angular dependence of the linewidth, which obeys anisotropy of the g-value. In the case of the charge order state, it should be in a non-magnetic state since there is no unpaired spin on the dimer. According to these results, it is considered that the remaining signal below T_{CO} comes from the residual spins, which could not form the CO state. In summary, the X = Et_2Me_2Sb salt shows a typical ESR behavior of the CO state.

The X = Me_4P ($t'/t = 0.62$), $EtMe_3Sb$ ($t'/t = 0.91$) and Et_2Me_2Sb ($t'/t = 1$) salts show

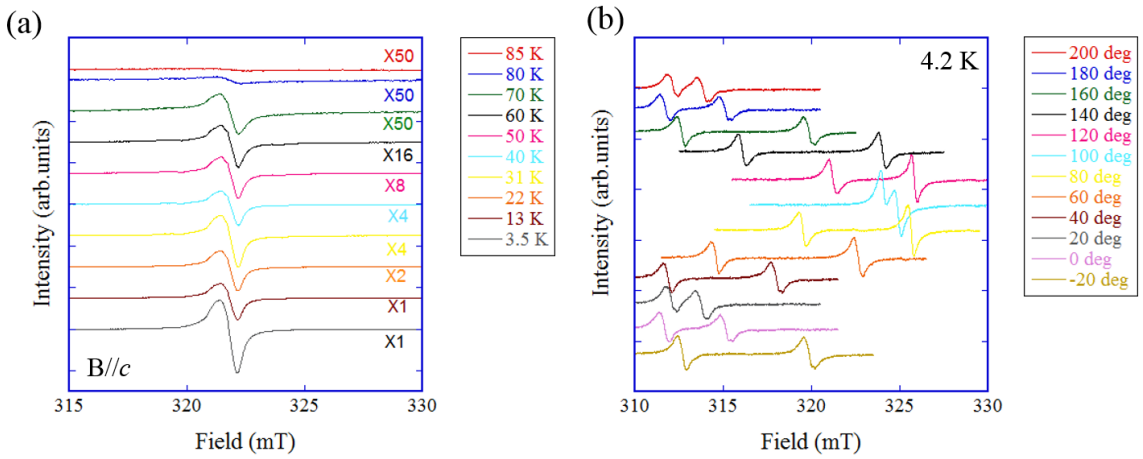

Figure 2.6: The ESR spectra of (a) the temperature dependence ($B//c$) and (b) the angular dependence ($B//ab$-plane) measurements for Et_2Me_2Sb salt.

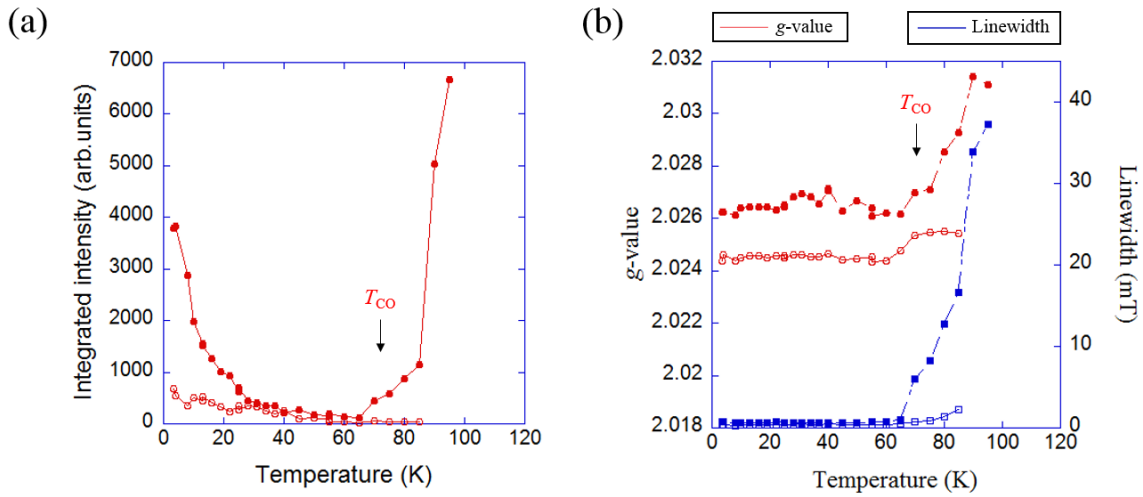

Figure 2.7: The temperature dependence of (a) the integrated intensity, (b) the g-value and the linewidth for Et_2Me_2Sb salt ($B//c$). The g-value and the linewidth are presented by red circles and blue squared.

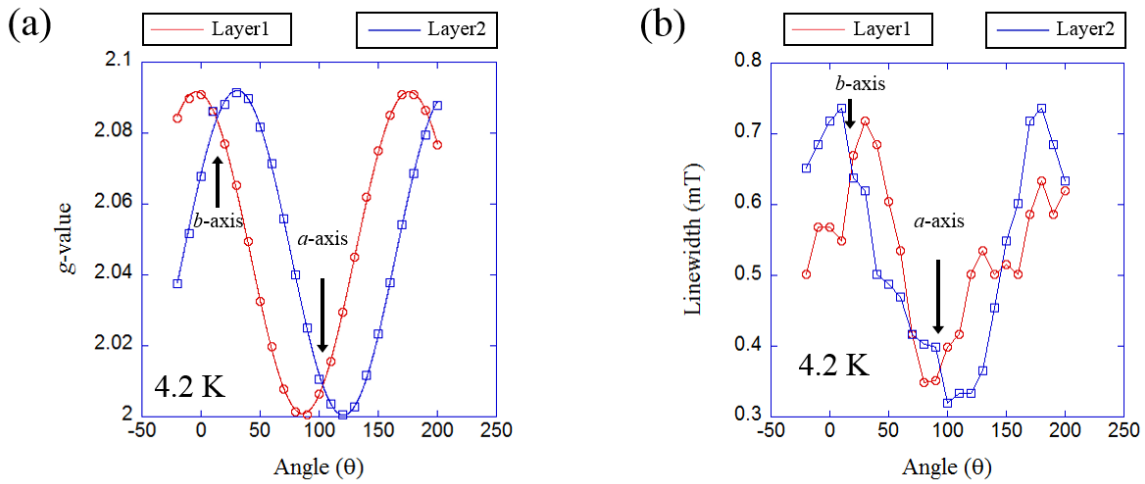

Figure 2.8: The angular dependence of the g-value and the linewidth for Et_2Me_2Sb salt ($B//ab$-plane). The red circle and blue circle is layer1 and layer2 signal, respectively.

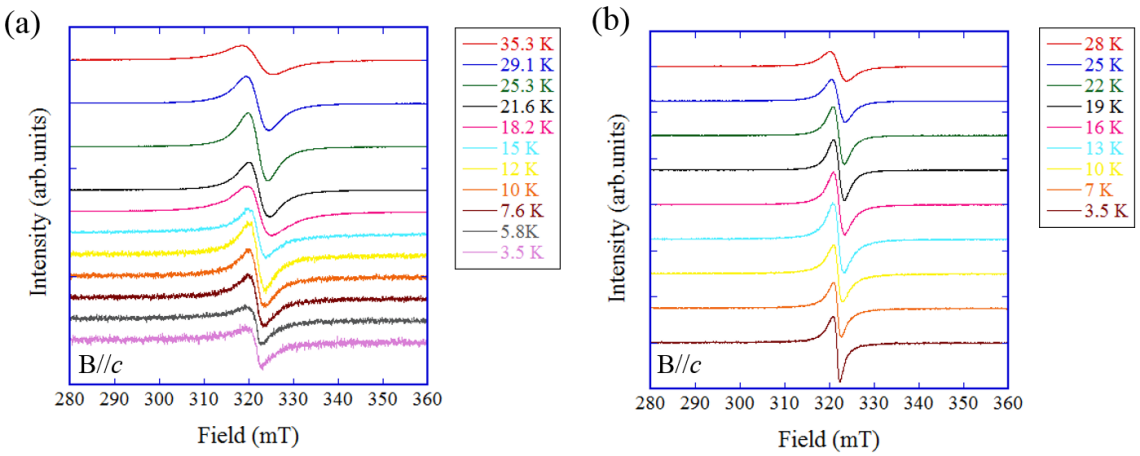

Figure 2.9: The ESR spectra of the temperature dependence for (a) Et_2Me_2P and (b) Me_4Sb salts ($B//c$).

typical ESR behavior of the antiferromagnetic state, spin liquid state and charge ordered state, respectively. Meanwhile, the X = Et_2Me_2P ($t'/t = 0.84$) and Me_4Sb ($t'/t = 0.86$) salts, which have the frustration parameter between the X = Me_4P and $EtMe_3Sb$ salts, show different ESR behaviors. Figures 2.9(a) and (b) are the typical ESR spectra for the X = Et_2Me_2P and Me_4Sb salts, respectively. The temperature dependence measurements have been performed for $B//c$-axis. In contrast to the X = Me_4P salt which is a typical antiferromagnet, the ESR signal of X = Et_2Me_2P and Me_4Sb salts do not disappear below T_N. Figures 2.10(a) and (b) are the temperature dependence of the ESR integrated intensity for both salts. The integrated intensity decreases around T_N, however, does not go to zero. As shown in Fig. 2.11, around

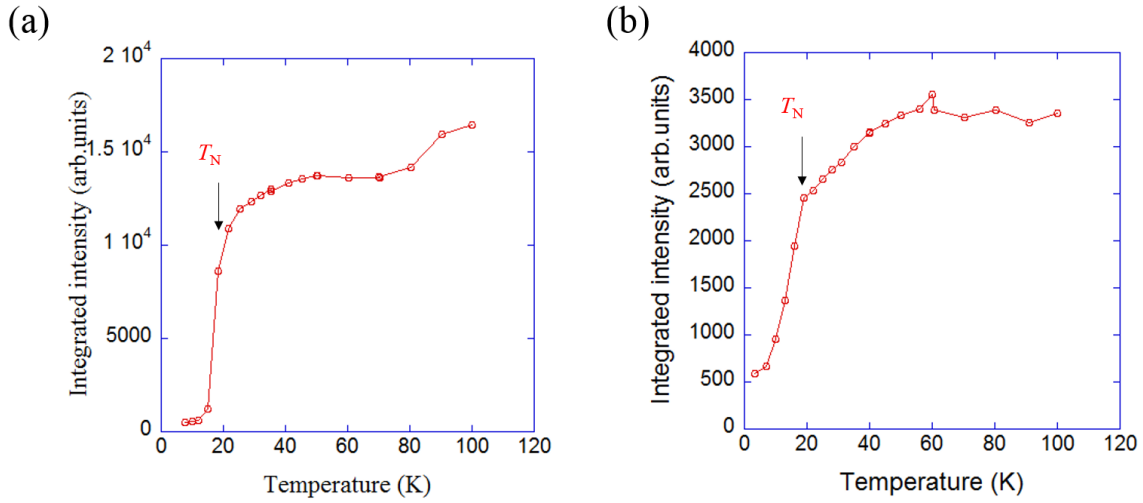

Figure 2.10: The Temperature dependence of the integrated intensity for (a) Et_2Me_2P and (b) Me_4Sb salts ($B//c$).

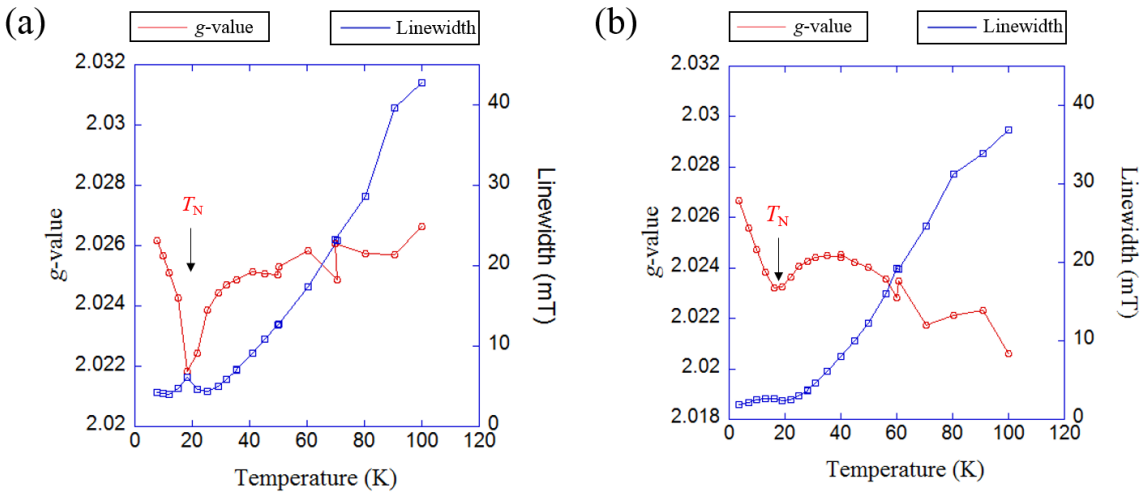

Figure 2.11: The Temperature dependence of the g-value and the linewidth for (a) Et_2Me_2P and (b) Me_4Sb salts ($B//c$).

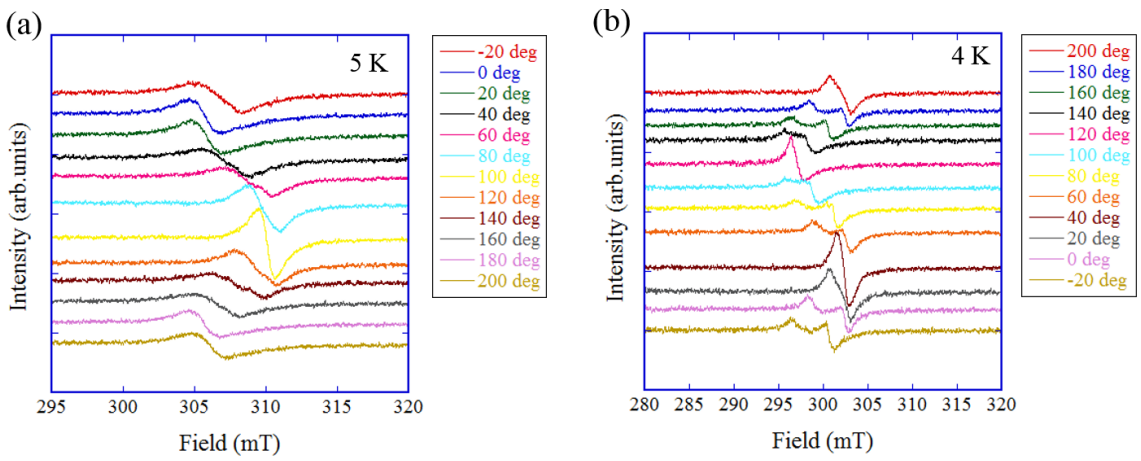

Figure 2.12: The ESR spectra of the angular dependence for (a) Et_2Me_2P and (b) Me_4Sb salts ($B//c$).

T_N, the g-value and the linewidth shows a dip and a peak around T_N, respectively.

These results cannot be explained by the typical antiferromagnetic behavior. The in-plane angular dependence of ESR has been performed to investigate the origin of the remaining signal at low temperature. Figure 2.12 is the typical ESR spectra for the angular dependence measurements for the X = Et_2Me_2P and Me_4Sb salts. The angular dependence measurements have been performed for $B//ab$-plane (i.e. parallel to the triangular lattice). Here, only a single ESR signal is observed for the result of the X = Et_2Me_2P salt, which does not reflect the solid cross column structure. This is probably due to the finite exchange interaction between Layer1 and Layer2. [51] In contrast, the X = Me_4Sb salt shows two ESR signals, which reflects the solid cross column structure. Figures 2.13 and 2.14 are the angular dependence of the g-value and linewidth for the X = $EtMe_2P$ and Me_4Sb salts, respectively. The angular dependence of g-value for the X = Et_2Me_2P and Me_4Sb salts obeys with the typical anisotropy of the g-value, but the linewidth shows different behavior with the empirical angular dependence of linewidth. The angular dependence of linewidth shows an enhancement along the diagonal direction of the triangular lattice similar to the X = $EtMe_3Sb$ salt (The QSL salt).

In order to get more information of residual signal of the X = Et_2Me_2P and Me_4Sb salts at low temperature, the V-band ESR measurement (about 58 GHz), which can observe antiferromagnetic resonance (AFMR) signal, has been performed. For comparison, the X = Me_4P salt, which has typical antiferromagnetic ground state, has been measured as shown in Fig. 2.15. From the result, the sharp signal, which is considered as EPR, is observed above

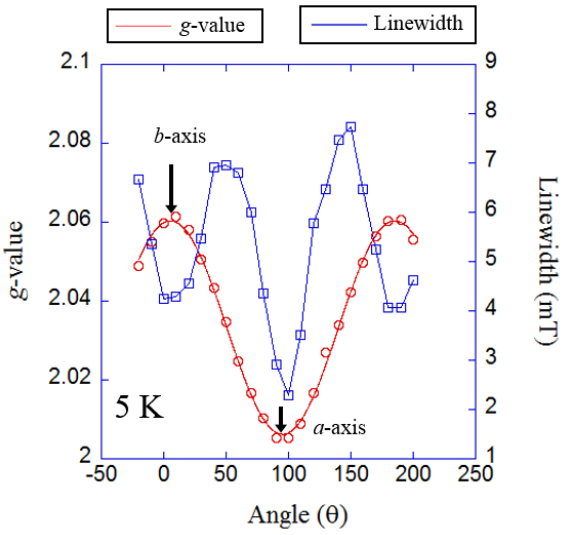

Figure 2.13: The temperature dependence of the integrated intensity for Et_2Me_2P salt. The g-value and the linewidth are presented by red circles and blue squared.

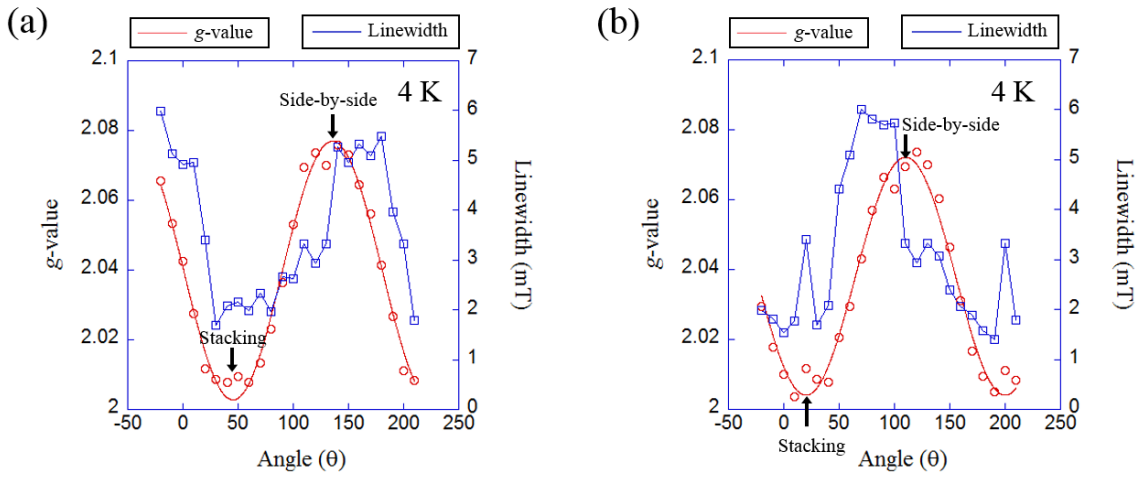

Figure 2.14: The temperature dependence of the integrated intensity for Me_4Sb salt. The g-value and the linewidth are presented by red circles and blue squared.

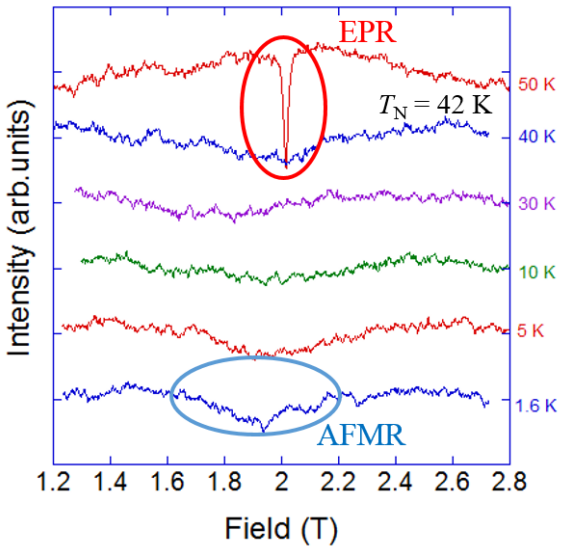

Figure 2.15: The ESR spectra of Me_4P salt using V-band ESR for $B//c$.

T_N = 42 K, and disappears below T_N. And the broad signal, which is considered as AFMR, appears below T_N. The broad AFMR signal is difficult to observe in X-band ESR, because it has a wide linewidth of about 300 mT as it can be seen in Fig 2.15 (blue oval).

However, the X = Et_2Me_2P and Me_4Sb salts show different behavior in the V-band ESR measurements. Figure 2.16(a) is the high-field ESR spectra for the X = Et_2Me_2P salt. The sharp signal, which is considered as the EPR signal, is observed above T_N, but remains below T_N. And the broad signal, which is considered as the AFMR, appears below T_N. When temperature decreases, the intensity of the sharp signal and the broad signal both increase. Therefore, it is considered that the EPR-like signal and the AFMR signal coexist below T_N. For the result of the X = Me_4Sb salt, the sharp signal is observed above T_N, and decreases below T_N. But the sharp signal does not disappear below T_N. And the broad signal appears below T_N, and increases as the temperature decreases. Thus, for the X = Me_4Sb salt case, the EPR-like signal and the AFMR signal also coexist below T_N. Although the X = Et_2Me_2P and Me_4Sb salts have similar behavior, the intensity of the sharp signal seems to be different at the lowest temperature. So, it is necessary to investigate accurately the absolute amount of spin contributing to the sharp signal.

The spin counting method, which is described in section 1.5.5, can investigate the absolute amount of spins. Thus, the spin counting method has been performed to investigate the

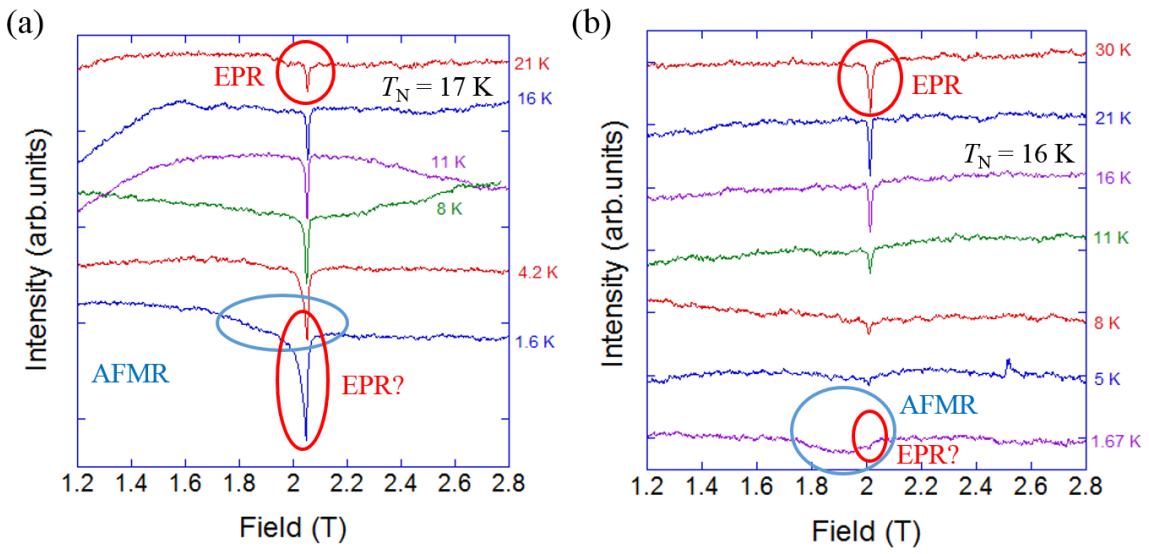

Figure 2.16: The ESR spectra of (a) Et_2Me_2P and (b) Me_4Sb salts using V-band ESR for $B//c$.

amount of the spin contributing to the sharp signal, which has similar behavior with the X = $EtMe_3Sb$ (QSL) salt. Figure 2.17(a) is the results of the spin counting. From the result, the amount of the spin is same at the highest temperature for all salts. For the case of the X = Me_4P salt, which has smallest frustration parameter $t'/t = 0.62$, the ESR signal disappear around T_N because it turns into the antiferromagnetic state. Hence, we could not obtain the amount of spin at the lowest temperature. For the X = Et_2Me_2P ($t'/t = 0.84$) and Me_4Sb salt ($t'/t = 0.86$), the amount of spin decreases at the transition temperature. And for the X = Et_2Me_2Sb salt, which has the CO ground state, the amount of spin decreases around T_{CO}. Figure. 2.17(b) is the relation between the frustration parameter t'/t and the amount of spin at 7 K. The amount of the remaining spin at 7 K is increasing by the increase of the frustration parameter t'/t, except for the X = Et_2Me_2Sb salt with a CO ground state. Therefore, the amount of residual spin at lowest temperature is thought to be related to the frustration parameter t'/t.

The experimental results will be discussed in the next section.

2.1.2 Discussions

As shown in the previous section, it is confirmed from the ESR measurements that the X = Me_4P, $EtMe_3Sb$ and Et_2Me_2Sb salts have the antiferromagnetic state, the spin liquid state, the charged ordered state, respectively. Meanwhile, the temperature dependence of the

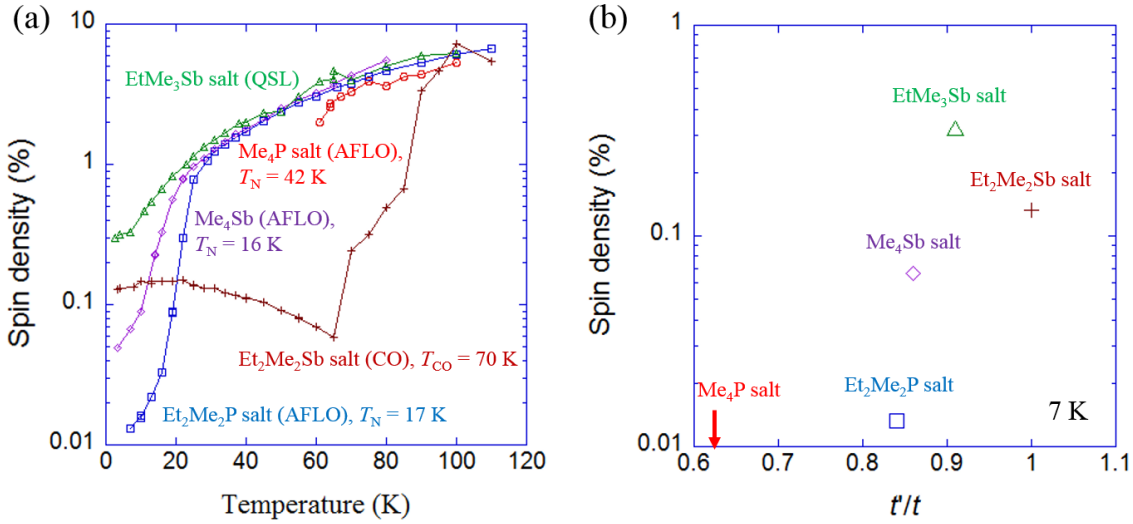

Figure 2.17: The spin counting results for Me_4P, Et_2Me_2Sb, Me_4Sb, $EtMe_3Sb$ and Et_2Me_2Sb salts using X-band ESR for $B//c$. (a) The temperature dependence of the spin counting results (b) The spin counting results at 7 K

linewidth for the X = $EtMe_3Sb$ salt shows the linewidth narrowing with the linear temperature dependence as shown in Fig. 2.3(b). The ESR linewidth is related with the spin-relaxation time T_1 and the spin-spin relaxation time T_2 according to Eq. 1.4 as described in Section 1.5.2. For the case of the motional narrowing, the contribution of the spin-spin relaxation time T_2 can be ignored, and only the spin-lattice relaxation time T_1 contributes to the linewidth. In a direct relaxation process, where the spin relaxation occurs by releasing one phonon, $1/T_1$ become proportional to temperature. Then, the linewidth becomes T-linear, $\Delta H_{1/2} \propto 1/T_1 \propto T$, when the motional narrowing occurs. [51–53] Hence, the T-linear behavior in the temperature dependence of the linewidth for the X = $EtMe_3Sb$ salt is considered to be due to the motional narrowing. In general, the first excitation of the spin liquid state is known as spinon. Therefore, the T-linear linewidth is a evidence of deconfined spin, and the origin of ESR can be considered to come from the spinon, which is the excited state of the QSL state. The QSL state of X = $EtMe_3Sb$ salt seems to be gapless since the spins seem to be deconfined from the T-linear behavior of linewidth. Moreover, the angular dependence of the linewidth of the X = $EtMe_3Sb$ salt does not obey with the empirical angular dependence, and the linewidth enhancement is observed when the field is applied along the diagonal direction of the triangular lattice (see Fig. 2.5 (left)). This anomaly of the angular dependence of the linewidth is considered to be due to the influence from the spin dynamics of the spinons.

On the other hand, the anomalous behavior is also observed at low temperature in the X = Et_2Me_2P and Me_4Sb salts, which is believed to have the antiferromagnetic ground state. In general, the EPR signal disappears below T_N in antiferromagnetic state. Then, the g-value and the linewidth decrease by decreasing the temperature, and a steep increase are both observed just above T_N. This steep increase of the g-value and linewidth above T_N is a typical precursor of antiferromagnetic long-range order, and is due to the development of antiferromagnetic correlation. However, the EPR-like signal is observed below T_N. Moreover, the temperature dependence of the g-value and the linewidth for the X = Et_2Me_2P and Me_4Sb salts shows a dip and a peak around T_N, respectively. This behavior is different from the behavior observed in a typical antiferromagnetic state. Moreover, in the results of the high-field ESR for th X = Et_2Me_2P and Me_4Sb salts, it is observed that the EPR-like signal and the AFMR signal coexisted below T_N. From the angular dependence of the linewidth (Figs. 2.13 and 2.14), the origin of the EPR-like signal is considered to be from the spinon, since the result is similar to the X = $EtMe_3Sb$ salt. However, the question remains whether the antiferromagnetic long-range order can be observed simultaneously with a spinon, which is the excitation of the spin-liquid state.

The spin counting measurements of X = Et_2Me_2P, Me_4Sb and $EtMe_3Sb$ salts were performed to investigate the amount of remaining spin, which is considered to be the spinon. The amount of the spin is the same at the highest temperature for all salts, and a decrease of the spin density is observed for the X = Et_2Me_2P, Me_4Sb salts around each transition temperature T_N. The amount of the spin density at the lowest temperature is increasing by the increase of the frustration parameter t'/t. From the above ESR results, it can be considered that the remaining spin of X = Et_2Me_2Sb salt is simply from the residual spin, and the remaining spin of the X = Et_2Me_2P, Me_4Sb and $EtMe_3Sb$ salts is considered to be from the spinon. Hence, it seems that the frustration parameter t'/t enhances the amount of the spinon.

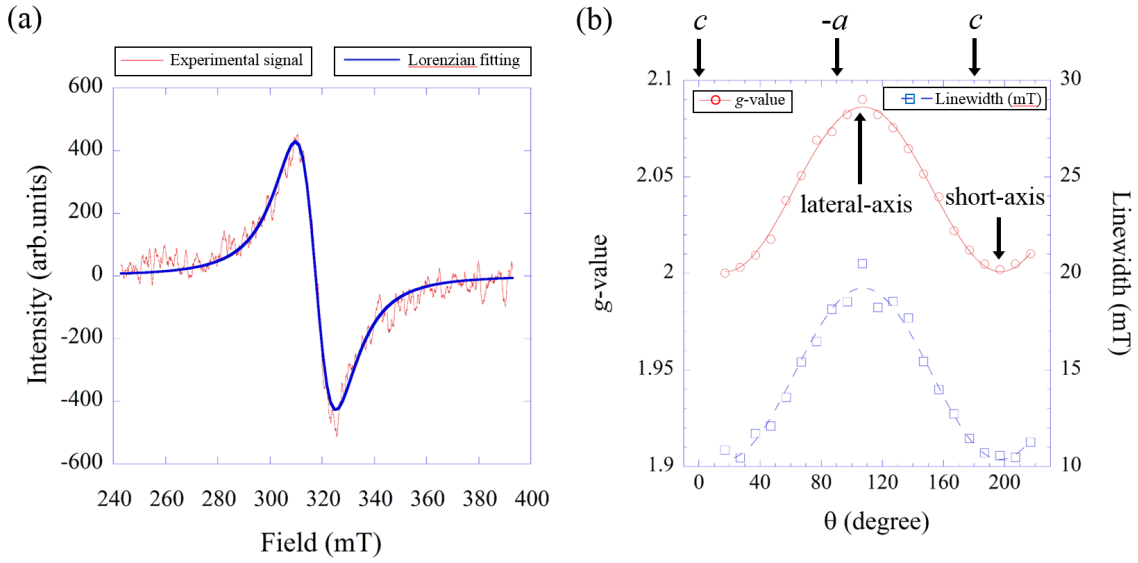

Figure 2.18: (a) Typical ESR signal at 44 K for $\theta = 107°$. The ESR spectrum is well fitted with a Lorentzian lineshape. (b) The angular dependence of g-value and linewidth at 44 K for $B//ac$-plane.

2.2 The X = $EtMe_3P$ salt (The valence bond solid state)

2.2.1 The ESR measurement results

First, the angular dependence of ESR was performed at 44 K to confirm the ESR origin. This temperature is above the VBS transition, and the ground state is considered to be in the paramagnetic state. Figure 2.18(b) is the angular dependence of the g-value and linewidth at 44 K for $B//ac$-plane (i.e. parallel to the triangular lattice). Here, the g-value and the ESR linewidth $\Delta H_{\rm pp}$ are presented by red open circles and blue open squares, respectively.

The angular dependence of the g-value, is well-fitted with the typical anisotropy of the g-value, $g_{\rm eff} = \sqrt{(g_{\rm max}^2 cos(\theta - \theta_{\rm max})^2 + (g_{min}^2 sin(\theta - \theta_{\rm max}))^2}$, where $g_{\rm max} = 2.086$, $g_{\rm min} = 2.001$ and $\theta_{\rm max} = 107°$. The ESR linewidth obeys the empirical angular dependence, $1 + \cos^2(\theta - \theta_{\rm max})$ with $\theta_{\rm max}$=107°, which is related to the magnetic anisotropy.

As shown in Fig. 2.18(b), the principal axes of the g-value, namely the maximum and minimum of g-value, are tilted 17° from the -a and c-axes, respectively. This angle mostly corresponds to the angle between the short-axis of the $Pd(dmit)_2$ dimer and the c-axis as shown in Fig. 1.30. It is known that g-value of the $Pd(dmit)_2$ dimer shows relatively large anisotropy due to Pd atoms, and the minimum and maximum of the g-values correspond to the short and lateral-axes of the $Pd(dmit)_2$ dimer, respectively. The angular dependence of

the g-value is consistent with the molecular arrangement of the Pd(dmit)$_2$ dimers as shown in Fig. 1.30, hence, it can be concluded that the origin of the ESR signal is the intrinsic spins of Pd(dmit)$_2$ dimers.

Next, the integrated intensity of the ESR signal, which is proportional to the spin susceptibility, is investigated. The open red circles in Fig. 2.19(a) are the temperature dependence of integrated intensity for $B//b$ (perpendicular to the triangular lattice). Here, the used frequency is about 9.12 GHz, and the resonance field is about 0.32 T. The ESR integrated intensity start to drop around 35 K, and becomes almost non-magnetic around 25 K. This is more or less consistent with the result of magnetic susceptibility claiming the VBS transition below 25 K. [45] As shown later, significant changes of g-value and linewidth, related to the VBS transition, are observed at 25 K.

A Curie-like contribution from residual spins, however, is also observed at the lowest temperature in Fig. 2.19(a). Such paramagnetic contribution is also observed in the magnetic susceptibility measurements, but generally subtracted, which is a conventional protocol for removing the contribution from impurities. As described later, this Curie-like contribution is from the spin excitations of the VBS state, and it should not be treated as a contribution from impurities. Therefore, it is not omitted in this thesis. The result of the integrated intensity in Fig. 2.19(a) is well reproduced by the following equation,

$$I = A_{\mathrm{VBS}} e^{-\frac{\Delta E}{k_B T}} + A_{\mathrm{res}} tanh(\frac{g\mu_B B \cdot S}{k_B T}) \tag{2.1}$$

The first term corresponds to the behavior of integrated intensity when a pair of $S = 1/2$ forms a valence bond (singlet state) and becomes exponentially non-magnetic with decreasing temperature. ΔE is the energy gap between the singlet and the triplet excited states. The second term is the contribution of residual spins, which is a general intensity behavior for unpaired spins ($S = 1/2$). A_{VBS} and A_{res} are proportional constants. The solid red curves in Fig. 2.19(a) are the fitting results using Eq. 2.1 with $\Delta E = 40$ and 90 K. The experimental data fits with the spin-gap of $\Delta E = 90$ K, and it is clear that $\Delta E = 40$ K, which is obtained from the magnetic susceptibility, does not reproduce the result in Fig. 2.19(a). [45] Note that the green and blue curves are the contribution of the first and the second term in Eq. 2.1 for $\Delta E = 90$ K, respectively.

To validate the obtained spin-gap, the magnetic field dependence was also performed.

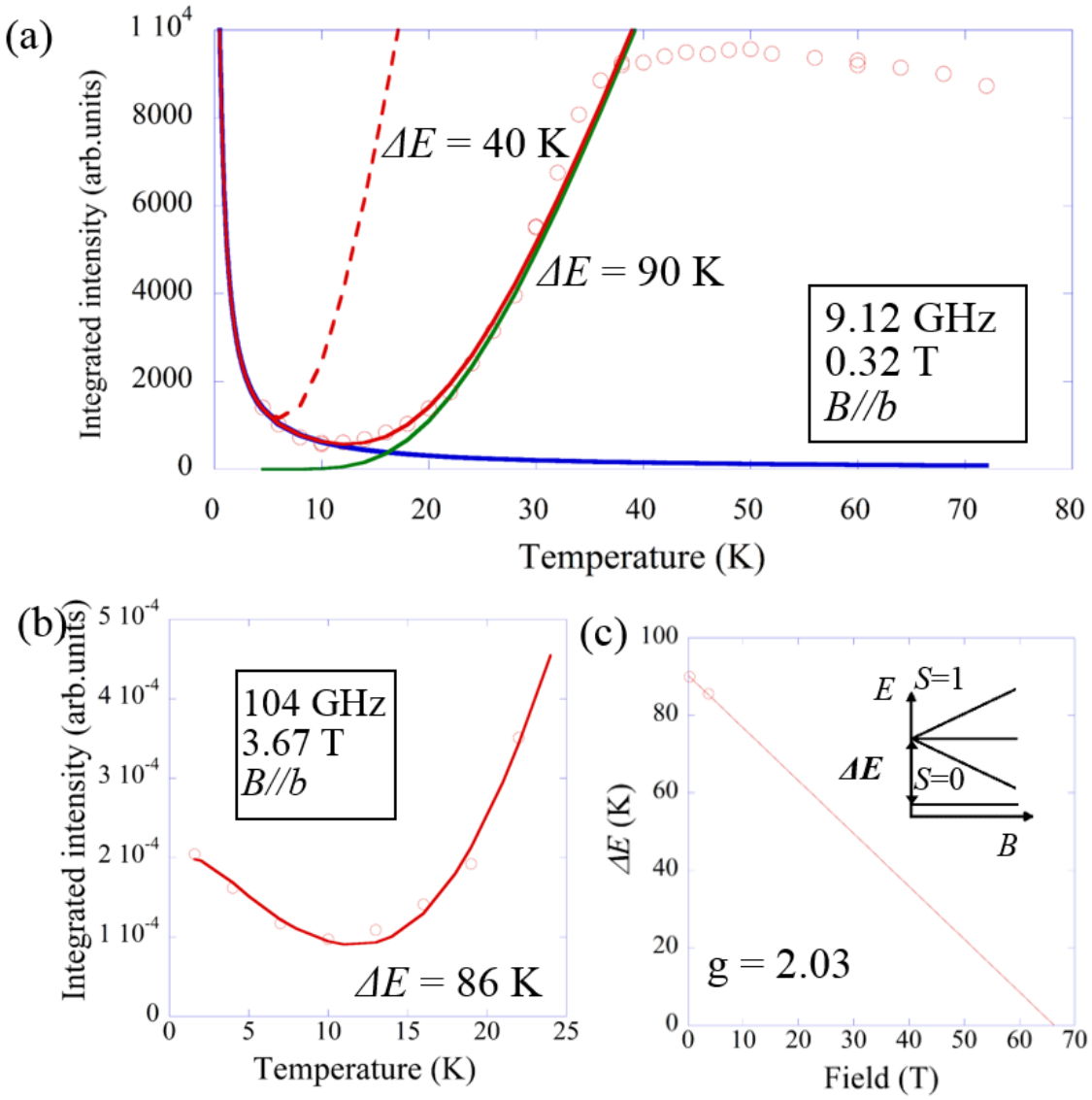

Figure 2.19: (a) Temperature dependence of integrated intensity using X-band ESR for $B//b$. Solid and dashed red lines are the fitting curves using Eq. 2.1 for $\Delta E = 40$ K and 90 K, respectively. blue and green solid curves are contributions from residual spins and valence bond formation, respectively. (b) Temperature dependence of integrated intensity using W-band ESR for $B//b$. Solid curve is the fitting for $\Delta E = 86$ K. (c) Field dependence of the spin-gap ΔE. Solid red line is the linear fitting using $g = 2.03$. The inset schematically represents the field dependence of the spin-gap ΔE.

The excited triplet state decreases with the magnetic field in accordance with the g-value as schematically shown in the inset of Fig. 2.19(c). Hence, ΔE should decrease with increasing the magnetic field. The temperature dependent integrated intensity for W-band ESR, where the used frequency was 104 GHz and the resonance field was 3.67 T, is shown in Fig. 2.19(b). From this result, $\Delta E = 86$ K from Eq. 2.1 is estimated. The magnetic field dependence of ΔE is plotted in Fig. 2.19(c). The spin gap follows the linear relation with $g = 2.03$, which coincides with the g-value of the applied direction of the magnetic field (i.e. the b-axis). Hence, it is concluded that the spin-gap of the VBS state in $EtMe_3P[Pd(dmit)_2]_2$ is 90 K.

It should be noted that the Curie-like contribution is much smaller in Fig. 2.19(b) than the contribution observed in Fig. 2.19(a). The ratio of the proportional constants $A_{\rm res}/A_{\rm VBS}$ are 0.143 and 0.014 for X-band and W-band, respectively. The ratio $A_{\rm res}/A_{\rm VBS}$ for X-band is ten times larger than that for W-band. Although the huge difference might be due to the lack of high temperature data in Fig. 2.19(b), the contribution of residual spins seems to depend on the magnetic field. Hence, residual spins observed at the lowest temperature should not be regarded as contribution from impurities.

In order to understand the origin of the low temperature ESR signal (i.e. residual spins), the temperature dependence of the ESR lineshape was investigated. As partly shown in Fig. 2.20(a), the ESR signal above $T_{\rm VBS} = 25$ K shows a typical Lorentzian lineshape, however, the ESR signal starts to show an asymmetric lineshape below $T_{\rm VBS}$. For example, the ESR spectra for 44 K in Fig. 2.18(a) and for 30 K in Fig. 2.20(b) fit well with the typical Lorentzian lineshape using Eq. 1.8 (see solid blue curves in Figs. 2.18(a) and 2.20(b)). On the other hand, the asymmetric ESR spectra for 4.8, 10, 20 K in Fig. 2.20(a) cannot be fitted neither with Lorentzian nor Gaussian lineshape. Such asymmetric lineshape reminds us of a Dysonian lineshape, which is usually observed in a metal. [54, 55] However, $EtMe_3P[Pd(dmit)_2]_2$ is a Mott insulator, and the adoption of Dysonian lineshape is ruled out. Then, it was assumed that the asymmetric lineshape observed below $T_{\rm VBS}$ is due to two ESR signals with different origins. The asymmetric ESR spectra was fitted using a double Lorentzian function, which is the sum of two different Lorentzian lineshapes. One of the fitting results is presented in Fig. 2.20(b) for the 4.8 K spectrum. The dashed purple and dotted green curves in Fig. 2.20(b) are the separated ESR signals with sharp and broad linewidth, respectively. The asymmetric lineshape is well reproduced by the sum of sharp and broad ESR signals with Lorentzian

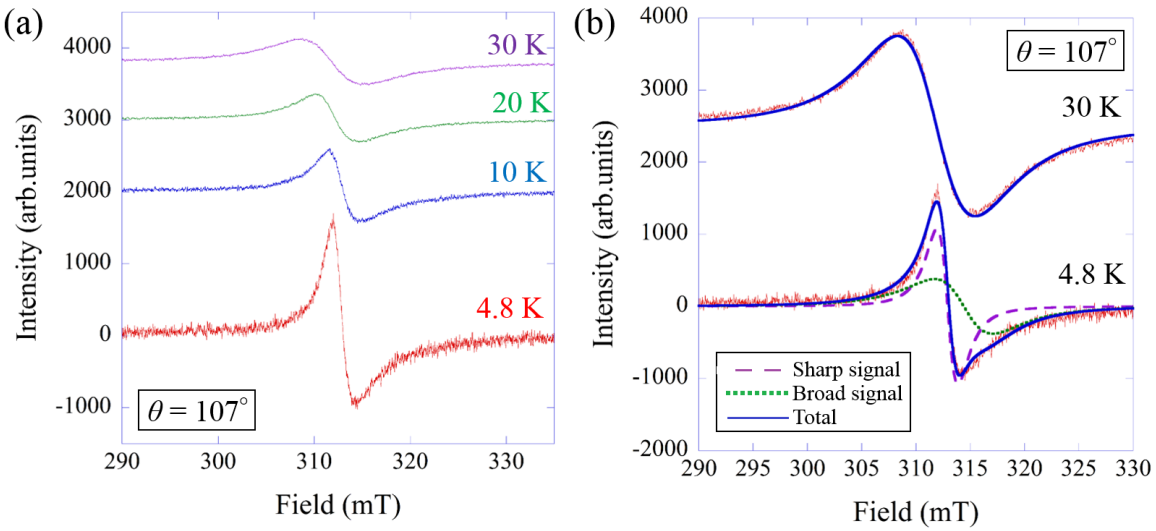

Figure 2.20: (a) Temperature dependence of typical ESR spectra for θ=107° ($B//g_{\max}$ in Fig. 2.18(b))). Asymmetric ESR lineshape appears below 25 K. (b) Fitting examples of the ESR signals. Although the ESR signal at 30 K can be fitted with a single Lorentzian (solid blue curve), the asymmetric ESR signal at 4.8 K can only be fitted with a double Lorentzian function (solid blue curve). Dashed purple an dotted green curves are the Lorentzian curves for sharp and broad signals, respectively.

lineshape (solid blue curve of the 4.8 K spectrum in Fig. 2.20(b)). The analysis indicates that spectrum fitting using a single Lorentzian is no more valid below $T_{\mathrm{VBS}} = 25$ K and the double Lorentzian fitting is needed to reproduce the observed ESR.

Temperature dependence of the g-value and the linewidth is presented in Figs. 2.21(a) and 2.21(b), respectively. The g-value and the linewidth were deduced from the fitting of the ESR spectrum for $\theta = 107°$ (g-value maximum in Fig. 2.18(b)). It is clear that the ESR observed above T_{VBS} remains even below T_{VBS} as a sharp ESR signal and new broad ESR signal appears below the VBS transition temperature. The appearance of this new broad signal seems to be the origin of the asymmetric ESR lineshape observed below T_{VBS}.

As one can see in Fig. 2.21(a), the g-value of the sharp signal is almost constant above T_{VBS}. The g-value starts to shift at T_{VBS} and becomes temperature-independent again below 12 K. The linewidth of the sharp signal constantly decreases, and a change of the slope is observed around T_{VBS} as shown in Fig. 2.21(b). The linewidth narrowing with the linear temperature dependence is also noticed below 18 K.

The temperature dependence of the broad signal, including the linewidth narrowing and the g-value, is slightly different from that of the sharp signal. Note that the constant g-value and the jump of the linewidth for the broad signal in the temperature range between 20 and

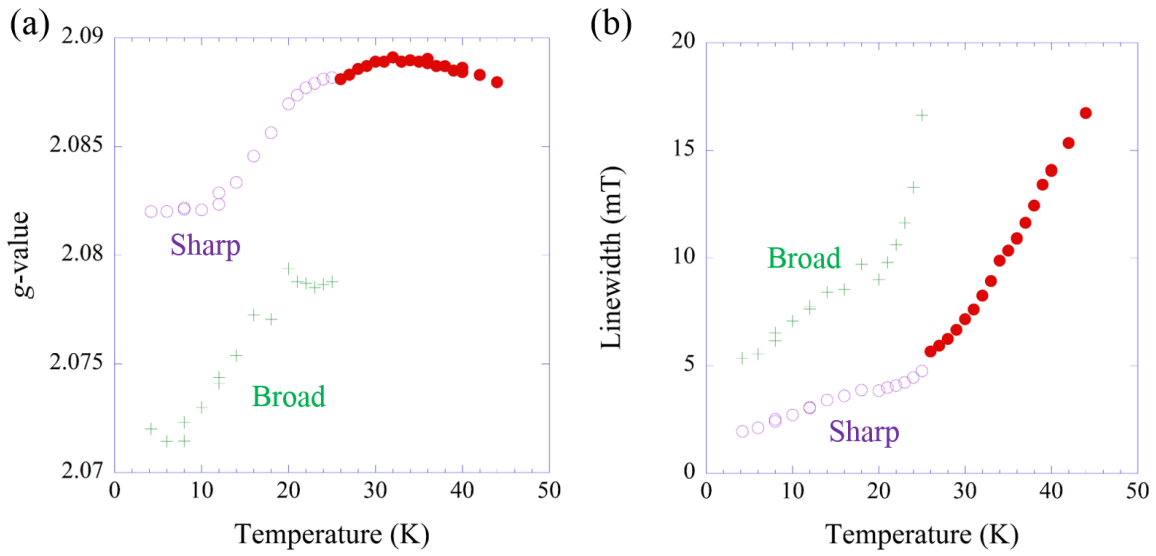

Figure 2.21: Temperature dependence of (a) g-value and (b) linewidth for $\theta = 107°$. Solid red circle symbols are the data obtained from the single Lorentzian fitting. Open purple circle and cross-shaped green symbols are the values for sharp and broad signal data obtained from the double Lorentzian fitting.

25 K might be due to some ambiguity since the intensity of the broad signal is extremely weak around T_{VBS}. The origin of these ESR signals is discussed in the next section.

In order to understand the spin dynamics of each ESR signal below T_{VBS}, the angular dependence of ESR at the lowest temperature was investigated. Figures 2.22(a) and 2.22(b) show the angular dependence of the g-value and linewidth obtained from the double Lorentzian fittings of the ESR spectra at 4.8 K. The g-value/linewidth for the sharp and broad ESR signals are given in Figs. 2.22(a) and 2.22(b), respectively. Although the minimum/maximum of the g-value are slightly different, the angular dependences of the g-value in Figs. 2.22(a) and 2.22(b) are similar to the result at 44 K in Fig. 2.18(b). From the fitting using $g_{\mathrm{eff}} = \sqrt{(g_{\mathrm{max}}^2 cos(\theta - \theta_{\mathrm{max}})^2 + (g_{min}^2 sin(\theta - \theta_{\mathrm{max}}))^2}$, g_{max} is 2.084 and 2.073, g_{min} is 2.000 and 1.995 for the sharp and broad signals, respectively. θ_{max} is 107° for both signals. Let us remind that $\theta_{\mathrm{max}} = 107°$ is also the result for the high temperature phase, hence, the anisotropy of the g-value is the same for 4.8 K and 44 K results. This suggests that the ESR origin is still from the spins on the $Pd(dmit)_2$ dimers.

On the other hand, the angular dependences of linewidth in Figs. 2.22(a) and 2.22(b) are quite different from the result for the high temperature phase shown in Fig. 2.18(b). As mentioned previously, the angular dependence of linewidth at 44 K, which is above T_{VBS}, has a

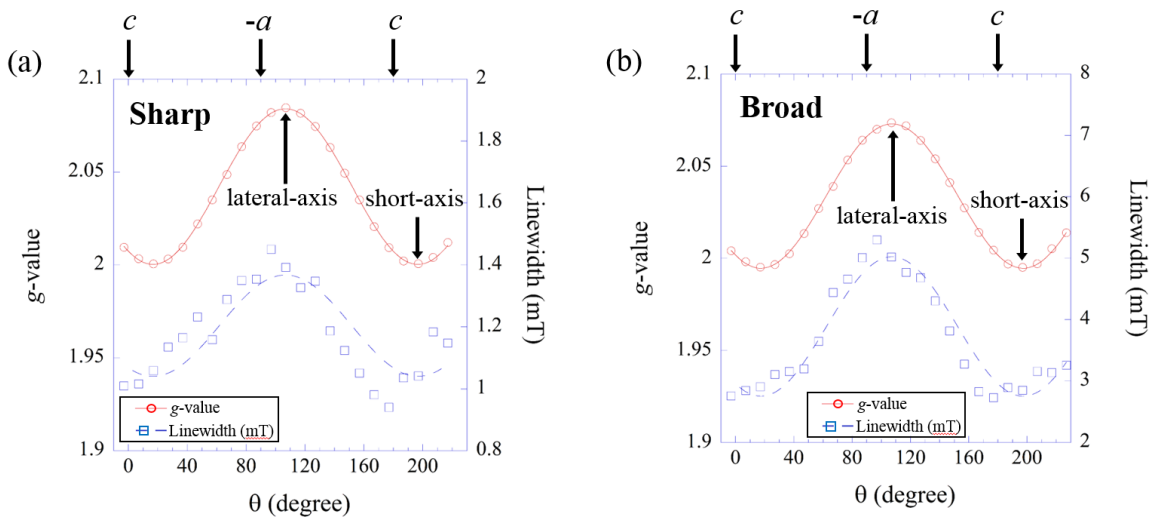

Figure 2.22: The angular dependence of the g-value and linewidth for (a) sharp and (b) broad signals at 4.8 K. The solid red and dashed blue curves are the fitting curves for the g-value and linewidth, respectively (see text).

$1 + \cos^2(\theta - \theta_{max})$ dependence reflecting the magnetic anisotropy of the system. However, the linewidth at 4.8 K, which is below T_{VBS}, does not fit with the $1 + \cos^2(\theta - \theta_{max})$ dependence, where θ_{max} was set with the same anisotropy with the g-value (i.e. $\theta_{max} = 107°$), as shown as dashed blue curves in Figs. 2.22(a) and 2.22(b) for the sharp and broad signals, respectively. Therefore, the spin dynamics of the residual spins seems to be quite different from the one in the high temperature phase.

The deviation of the experimental data from the $1 + \cos^2(\theta - \theta_{max})$ dependence (dashed blue curves in Figs. 2.22(a) and 2.22(b)) gives us two kinds of important information, (i) the spin dynamics for both signals changes at the VBS transition, and (ii) the spin dynamics is different between the sharp and broad signals since the largest deviation of the linewidth from the $1 + \cos^2(\theta - \theta_{max})$ dependence is observed around g_{min} and g_{max}, respectively. Let us remind that g_{min} is along the short-axis and g_{max} is along the lateral-axis of the dimer.

It is known that some interesting spin dynamics is observed in the spin-Peierls system. For example, in a famous spin-Peierls system $CuGeO_3$, a two-spinon continuum accompanied by a gap is observed along the chain direction, and spin dynamics along the transverse direction of the chain is also observed. [56,57] Such transverse dynamics is considered to be due to the poor one dimensionality (1D) of the spin chain in $CuGeO_3$, but there is no clear theoretical answer to date. It is known that the angular dependence of the ESR linewidth shows $(3\cos^2\theta - 1)^{4/3}$

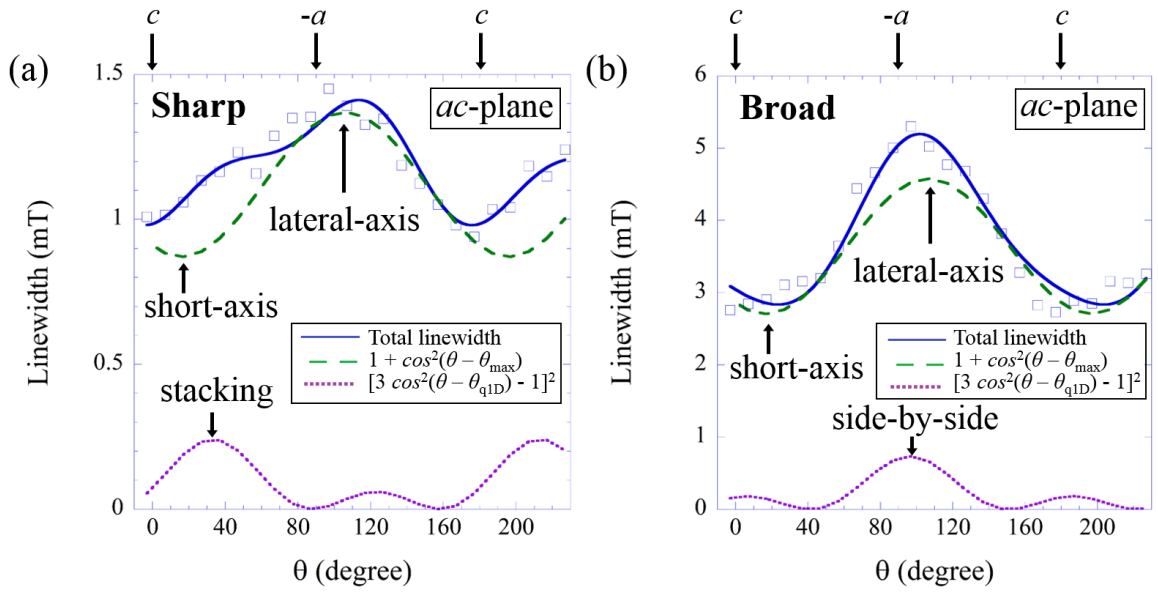

Figure 2.23: Angular dependence of ESR linewidth for (a) sharp and (b) broad signals at 4.8 K analyzed with additional q1D spin dynamics. The dashed green and dotted purple curves are $1 + \cos^2(\theta - \theta_{\mathrm{max}})$ and $(3\cos^2(\theta - \theta_{\mathrm{q1D}}) - 1)^2$ dependences, respectively. The solid blue curve is the sum of the two functions.

and $(3\cos^2\theta - 1)^2$ dependences for pure 1D and quasi-1D (q1D) spin system. [58–61] Since the VBS state is similar to the spin-Peierls state, it was assumed that additional low-dimensional spin dynamics might be hidden in the angular dependence of the ESR linewidth.

Figures 2.23(a) and 2.23(b) are new fitting results for the angular dependence of the ESR linewidth at 4.8 K. Here, the $(3\cos^2\theta - 1)^2$ dependence, which corresponds to the q1D spin dynamics, is added to the empirical $1 + \cos^2(\theta - \theta_{\mathrm{max}})$ dependence reflecting the magnetic anisotropy. Here, θ_{max} is fixed to 107° since the latter angular dependence should coincide with the anisotropy of the g-value. Meanwhile, θ_{q1D} is left as a free parameter for the fitting. As shown as solid blue curves in Figs. 2.23(a) and 2.23(b), the fitting results including the q1D spin dynamics reproduce the angular dependence of the sharp and broad signals better than Figs. 2.22(a) and 2.22(b) where only the $1 + \cos^2(\theta - \theta_{\mathrm{max}})$ dependence is taken into account. To elucidate each contribution, the former and the latter angular dependences are presented separately as dotted purple and dashed green curves, respectively (Fig. 2.23).

The angle θ_{q1D} is the direction of the q1D dynamics. As shown as the dotted purple curves in Figs. 2.23(a) and 2.23(b), $\theta_{\mathrm{q1D}} = 33°$ (for the sharp signal) and $\theta_{\mathrm{q1D}} = 96°$ (for the broad signal) are obtained. These angles seem slightly different from the minimum/maximum angles in the $1 + \cos^2(\theta - \theta_{\mathrm{max}})$ dependence. These θ_{q1D} values (33° and 96°) correspond to

the directions mostly along the c-a and a-axis, respectively. These results suggest that the ESR signals with the sharp and broad linewidth have additional q1D spin dynamics along different directions, along the stacking and the side-by-side directions of the $Pd(dmit)_2$ dimers, respectively. The origin of these dynamics is discussed in the next section.

2.2.2 Discussions

A spin-gap feature in the integrated intensity of ESR around 25 K have been observed as shown in Fig. 2.19(a). The results indicate that the spin gap ΔE is 90 K, which is about 2.3 times larger than the value obtained from previous studies. [45, 48] In this first part of this section, the spin-gap obtained from the ESR results will be discussed.

From the magnetic susceptibility measurement, the high temperature phase of $EtMe_3P[Pd(dmit)_2]_2$ can be considered as an antiferromagnetic triangular lattice system with the exchange energy of about J = 250 K. [45] Then, the system turns into the VBS state by deforming the lattice at 25 K. There are only few 2D materials, such as CaV_4O_9 and $SrCu_2(BO_3)_2$, which have a singlet ground state. [62, 63] The latter compound is good realization of the Shastry-Sutherland model. However, the singlet ground state is formed without breaking any lattice symmetry for both compounds. Hence, these 2D compounds cannot be directly compared with $EtMe_3P$ salt. Hereinafter, results of this thesis are compared with the spin-Peierls system, which is observed only in a 1D system but has the singlet state induced by breaking the lattice symmetry.

Using the mean-field approximation for the spin-Peierls system, a linear relation $\Delta E \approx 1.64(2J)\delta$ is predicted, where δ corresponds to the distortion of exchange energies due to the double periodicity along the chain, $J_1 = J(1 + \delta)$, $J_2 = J(1 - \delta)$. [57,64] $\delta = 0.11$ was obtained from the above relation for J = 250 K and ΔE = 90 K. This value of $\delta = 0.11$ is very close to the value of organic spin-Peierls materials, such as TTF-CuBDT (TTF = tetrathiafulvalene, BDT = bis-cis-(1,2-perfluoromethylethylene-1,2-dithiolate)), MEM-$(TCNQ)_2$ (MEM = N-methyl-N-ethyl-morpholinium, TCNQ = tetracyanoquinodimethanide), and D-F_5PNN (deuterated pentafluorophenyl-nitronyl-nitroxide), where δ is between 0.08 and 0.2. [65, 66] In contrast, δ for an inorganic spin-Peierls system $CuGeO_3$ is 0.06. [56,57] The similarity of δ in the organic spin-Peierls system is supposed to be due to the flexible nature of organic molecules.

On the other hand, the relation between the transition temperature and the spin-gap de-

viates from that of the typical spin-Peierls system. In the mean-field approximation, a relation of $2\Delta E/T_{\rm sp} \approx 3.53$ ($T_{\rm sp}$: spin-Peierls transition temperature) is expected, which results from the treatment of the spin-phonon interaction in the weak-coupling limit. [57, 64] The experimental values for $2\Delta E/T_{\rm sp}$ fall in the range of $3.2 \sim 3.5$ for typical spin-Peierls compounds. Meanwhile, a relatively high ratio $2\Delta E/T_{\rm VBS} = 7.2$ was obtained for $EtMe_3P[Pd(dmit)_2]_2$. Such a large ratio of $2\Delta E/T_{\rm sp} \sim 6$ was previously observed for α'-NaV_2O_5 and D-F_5PNN, where a charge ordered state or the intra-molecular spin polarization is the origin of the large ratio. [66–69] For $EtMe_3P[Pd(dmit)_2]_2$, an intradimer charge disproportionation below $T_{\rm VBS}$ is observed from the vibrational spectroscopy. [70] Hence, the large ratio observed in $EtMe_3P[Pd(dmit)_2]_2$ might be due to the polarization inside the $Pd(dmit)_2$ dimer, or the relation $2\Delta E/T_{\rm sp} \approx 3.53$ is just not valid for the VBS state.

In principle, ESR should not be observed in the VBS state, since it is a spin singlet state. In the case of $EtMe_3P[Pd(dmit)_2]_2$, however, ESR was still observed below $T_{\rm VBS}$ and the spin susceptibility exhibited a Curie-like feature (Fig. 2.19(a)). Such a Curie contribution is usually removed from the raw data of static magnetic susceptibility since it is considered as a contribution from impurities. However, the angular dependence of the g-value at 4.8 K suggests that the ESR origin below $T_{\rm VBS}$ is still the $Pd(dmit)_2$ dimer (Figs. 2.22(a) and 2.22(b)), and a characteristic low-dimensional spin dynamics was found from the angular dependence of ESR linewidth (Figs. 2.23(a) and 2.23(b)). These results indicate that the observed ESR below $T_{\rm VBS}$ and the Curie component in the magnetic susceptibility contain some important information about the excited states of the VBS state. Next, the low-energy spin excitations of the VBS state, and its characteristic spin dynamics in the low temperature phase below $T_{\rm VBS}$ will be discussed.

As mentioned in the previous section, the observation of the asymmetric ESR lineshape below $T_{\rm VBS}$ is due to two (sharp and broad) ESR signals. The sharp ESR signal seems the same as that observed in the high temperature phase (i.e. above $T_{\rm VBS}$), because both g-value and linewidth are continuous at $T_{\rm VBS}$ (Figs. 2.21(a) and 2.21(b)). In contrast, the g-value and linewidth of the broad ESR signal are different from those of the sharp one, and appears only below $T_{\rm VBS}$). Considering that the ESR observed in the high temperature phase is from the spin ($S = 1/2$) on the $Pd(dmit)_2$ dimer, the sharp ESR signal is expected to originate from the residual spins that cannot form the valence bond below $T_{\rm VBS}$. In contrast, the broad ESR

signal is a signal related with the appearance of the VBS state.

As mentioned above, the sharp signal is supposed to come from an unpaired spin ($S = 1/2$). The g-shift observed between 12 and 20 K is probably due the decrease of spin correlation since the number of neighboring spins with $S = 1/2$ exponentially decreases owing to the formation of the valence bonds. The g-value becomes temperature independent below 10 K since the residual spins are far away from each other. Meanwhile, the sharp signal observed above $T_{\rm VBS}$ has a typical angular dependence of linewidth related to the magnetic anisotropy (Fig. 2.18(b)), and an additional q1D feature appears below $T_{\rm VBS}$ along the stacking direction of the dimers (Fig. 2.23(a)). These results suggest that the localized spins on the $Pd(dmit)_2$ dimers becomes mobile below $T_{\rm VBS}$, like solitons. The existence of mobile spins is confirmed from the T-linear narrowing of the ESR linewidth observed below 18 K for the sharp signal in Fig. 2.21(b), which is a typical ESR behavior due to the motional narrowing. [51–53] According to the angular dependence of ESR linewidth in Fig. 2.23(a), the q1D spin dynamics is along the stacking direction of the dimers, where alternated exchange interactions are expected due to the alternated interdimer spacing in this direction. This situation is similar to the spin-Peierls compounds, where a soliton excitation is observed for TTF-AuBDT, D-F_5PNN and (DMe-DCNQI)$_2$Li (DMe-DCNQI = dimethyl-dicyanoquinone-diimine), except that transverse exchange interactions also exist in $EtMe_3P[Pd(dmit)_2]_2$ owing to the triangular lattice network. [71–73]

Nakano and Fukuyama predicted a soliton excitation for the spin-Peierls systems. [74] Although it is not clear if it is also applicable for the VBS system, it is known that the soliton excitation energy $\Delta E_{\rm sol}$ is considerably lower than the triplet excitation energy ΔE, where the approximate relation is $\Delta E_{\rm sol} \sim 0.3\Delta E$. [71] Assuming that the soliton picture is valid, $\Delta E_{\rm sol} = 27$ K is expected for the present system. This value is consistent with observation of this thesis since the T-linear narrowing of linewidth, which is due to the motional narrowing of deconfined spins, is observed below 18 K. Therefore, it is proposed that the origin of the sharp ESR signal observed below $T_{\rm VBS}$ is the soliton excitation ($S = 1/2$) in the VBS state.

On the other hand, the broad ESR signal shows different behavior compared with the sharp one. The temperature dependence is slightly different (Figs. 2.21(a) and 2.21(b)), and the q1D dynamics is observed along the side-by-side direction of the $Pd(dmit)_2$ dimers (Fig. 2.23(b)). The first candidate for its origin is another soliton excitation, which is propagated

along the side-by-side direction. However, there is no reason why the ESR behavior (e.g. T-dependence of g-value or linewidth) is different from that of the sharp one, because the signal should come from the same unpaired spin. The second candidate is the excited triplet state ($S = 1$) of the VBS state. This makes more sense, since the ESR origin is now $S = 1$ bosons, and the g-value and the linewidth are expected to be different from those of the sharp one. Since the spin-gap is 90 K, however, the contribution from the triplet excitation is supposed to decrease with temperature and the ESR should be very small at 4.8 K. Assuming that the aforementioned soliton excitation exists, it is also possible that the $S = 1$ triplet state is formed by the pairing of solitons ($S = 1/2$) with the elastic restoring force in the VBS state. In this case, however, there is no clear explanation for the q1D dynamics along the side-by-side direction, while the solitons seem to be propagated along the stacking direction.

The third candidate is the collective spin excitation of the magnons (i.e. spin-wave excitation $\Delta S = 1$). Saito and Fukuyama theoretically predicted that there are two kinds of magnetic excitations, the gapped triplet excitation and the gapless spin-wave excitation, in the disordered spin-Peierls system (i.e. spin-Peierls system doped with impurities). [26] It is supposed that the randomly distributed residual spins (or solitons) will have the same effect on the system. The number of spins that remain at the lowest temperature by using the spin counting method of ESR was studied. By comparing the integrated intensity of the standard sample $CuSO_4{\cdot}5H_2O$, The amount of the residual spins is estimated that remain at 4.8 K to be about 0.13 % of the total spins. This spin density corresponds to the distance of 32 dimer sites between the residual spins, when 2D network is considered. In such a condition, the gapped triplet excitation and the gapless spin-wave excitation can coexist. [26] As mentioned above, the ESR observation of the excited triplet state seems unlikely due to the huge spin-gap. Hence, it is proposed that the broad ESR signal is due to the spin-wave excitation ($\Delta S = 1$), which is essentially a collective spin excitation of the magnons. This does not contradict with the observation of ESR signal at the lowest temperature, because such a spin excitation is expected to be gapless. The behavior of the g-value and the linewidth is expected to be different from those of the sharp ESR signal that originates from the different spin excitation.

Chapter 3

Conclusion

The anion radical salts β'-X[Pd(dmit)$_2$]$_2$ (X = Me_4P, Et_2Me_2P, Me_4Sb, $EtMe_3Sb$ and Et_2Me_2Sb), which have triangular lattice, was studied by ESR. First, the temperature dependence of ESR measurements for the X = Me_4P salt (t'/t = 0.62), which is believed to have the antiferromagnetic ground state, shows a steep increase of g-value and linewidth just above T_N. And ESR signal disappears below T_N. According to these results, the X = Me_4P salt shows a typical ESR behavior of the antiferromagnetic state.

Next, the temperature dependence of ESR measurements for the X = $EtMe_3Sb$ salt (t'/t = 0.91), which is the candidate material for the spin liquid ground state, shows the linewidth narrowing with a linear temperature dependence at low temperature. This T-linear dependence of linewidth is a evidence of deconfined spin, and the origin of ESR can be considered to come from the spinon, which is the excited state of the QSL state. Hence, the QSL state of X = $EtMe_3Sb$ salt seems to be gapless from this study. Moreover, the angular dependence of the linewidth for B//triangular lattice does not obey with the empirical angular dependence, and the enhancement of the linewidth is observed when the field is applied along the diagonal direction of the triangular lattice. From these results, it is considered that there is spin dynamics along the diagonal direction, which additionally contributes to the linewidth.

Next, temperature dependence of the X = Et_2Me_2Sb salt (t'/t = 1), which is believed to have the charged ordered ground state, shows that the g-value and the linewidth decrease above T_{CO}, and become temperature independent below T_{CO}. The integrated intensity rapidly decreases around T_{CO}, but the spin remains at low temperature. The angular dependence of linewidth is well-fitted with the typical angular dependence of linewidth. Thus, it is

considered that the remaining signal below T_{CO} comes from the residual spins, which could not form the CO state. According to these results, the X = Et_2Me_2Sb salt shows a typical ESR behavior of the CO state.

The X = Me_4P, $EtMe_3Sb$ and Et_2Me_2Sb salts shows a typical ESR behavior of the antiferromagnetic state, spin liquid state and charge ordered state, respectively. Meanwhile, the X = Et_2Me_2P (t'/t = 0.84) and Me_4Sb (t'/t = 0.86) salts, which have the frustration parameter between the X = Me_4P, $EtMe_3Sb$ salts, show different ESR behaviors. The ESR integrated intensity decreases around T_N, however, does not go to zero. Furthermore, the angular dependence of the linewidth for B//triangular lattice shows also an anomalous behavior, which resembles with the angular dependence of the linewidth for the X = $EtMe_3Sb$ salt. This suggests the possibility that the spinon also exists in the X = Et_2Me_2P and Me_4Sb salts. Meanwhile, the high-field ESR measurements for the X = Et_2Me_2P and Me_4Sb salts showed the coexistence of the EPR-like signal and the AFMR signal below T_N. Considering the angular dependence which shows an enhancement for B//diagonal direction, it is most probable the observed EPR-like signal is due to the same signal observed for the X = $EtMe_3Sb$ (QSL) salt (i.e. spinon).

In order to investigate the amount of remaining spin contributing to the anomalous behavior, the spin counting method has been performed. From the result, the amount of the spin is same at the highest temperature for all salts, and X = Me_4P, Et_2Me_2P, Me_4Sb and Et_2Me_2Sb salts decrease around each transition temperature. The amount of the remaining spin at the lowest temperature is increasing by the increase of the frustration parameter t'/t, except for the X = Et_2Me_2Sb salt with a CO ground state. From the above ESR results, it is considered that the remaining spin of X = Et_2Me_2Sb salt is simply from the residual spin, and the remaining spin of the X = Et_2Me_2P, Me_4Sb and $EtMe_3Sb$ salts is considered to be from the spinon. Thus, the amount of spinon is considered to be related with the frustration parameter t'/t.

On the other hand, the low-temperature spin dynamics of the VBS state in $EtMe_3P[Pd(dmit)_2]_2$ was studied by ESR. From the temperature dependence of the ESR's integrated intensity, the spin-gap ΔE = 90 K was estimated. Although a typical Lorentzian ESR lineshape was observed in the high temperature phase, the ESR lineshape became asymmetric below T_{VBS}, which is due to two independent ESR signals with different linewidth. It

is proposed that the origins of the observed ESR signals with sharp and broad linewidth are the soliton excitation ($S = 1/2$) and the spin-wave excitation ($\Delta S = 1$) of the VBS state, respectively.

Although some candidates are lined up based on the spin excitations found in the spin-Peierls system, it is not yet clear that these excitations observed in the spin-Peierls system are also applicable to the VBS system. It is hoped that this findings initiate some new theoretical studies about the elementary excitation in the VBS state.

There remain a few open questions to be answered at this stage. In this thesis, the sharp ESR signal has been attributed a spin excitation of the soliton (i.e. deconfined $S = 1/2$). However, the reason why the q1D spin dynamics is observed along the stacking direction and not along the transverse direction is not so clear. Since solitons are driven by the phonons and can be propagated by locally distorting the lattice, it might suggest that the energy cost for the molecular displacement in this system is smaller along the stacking direction rather than the side-by-side direction. Furthermore, the broad signal has been also attributed the spin-wave excitation, but it is not clear either that the q1D spin dynamics is observed along the side-by-side direction. Thus, theoretical studies of the spin dynamics are also highly desired.

Another open question is the effect of the magnetic field. For the spin-Peierls system, it is known that solitons and excited triplet bosons are more easily formed in higher magnetic region since the spin-gap decreases with the increase of the magnetic field. [71,74] However, the low temperature ESR contribution, which is the sum of the soliton and spin-wave excitations, seems rather small for the W-band ESR as shown in Fig. 2.19(b) (corresponding the magnetic field of 3.67 T). The reason for such small ESR intensity is unknown at this stage, and more precise high field ESR measurement is needed for the future.

Finally, it is an open question why the QSL state does not appear for the β'-X[Pd(dmit)$_2$]$_2$ salt with $t'/t = 1$. In general, antiferromagnetic triangular lattice ($t'/t = 1$) is the most frustrated system, and QSL state should appear. However, the X = Et_2Me_2Sb salt (CO state) and $EtMe_3P$[Pd(dmit)$_2$]$_2$ (VBS state) with $t'/t = 1$ show two ground states which are both accompanied with a lattice deformation. These results might suggest that it is energetically more favorable to achieve a gapped ground state by deforming the lattice rather than keeping the highly degenerated QSL ground state for $t'/t = 1$. Meanwhile, the difference of ground state between the X = Et_2Me_2Sb salt and the $EtMe_3P$[Pd(dmit)$_2$]$_2$ is coming from different

structures, which are the solid-cross column structure and the parallel column structure, respectively. Lattice defromation along the c-a axis is easier for the $EtMe_3P[Pd(dmit)_2]_2$ salt, which has a parallel column structure, and interdimer valence bonds are easily formed to achieve the VBS state. On the other hand, the X = Et_2Me_2Sb salt can not make structural deformation on one-axis due to the solid cross column structure, which leads to a CO state with only intradimer deformations.

Acknowledgements

I would like to express sincere gratitude to my advisor Prof. Y. Oshima for many advices and valuable discussions. I grateful to Prof. A. Kawamoto, Prof. H. Amitsuka and Prof. K. Ichimura for accepting to be the referee of this thesis. I would like to thank to Dr. R. Kato for providing me many attractive samples, valuable discussions. I would like to express gratitude to Dr. S. Fujiyama for valuable discussions. I would like to thank all members of Kato laboratory. Finally, I would like to thank my family for their support.

References

[1] S. Blundell. *Magnetism in Condensed Matter*. Oxford, (2001).

[2] P. W. Anderson. *Mater. Res. Bull.*, **8**:153, (1973).

[3] N. Achiwa. *J. Phys. Soc. Jpn.*, **27**(3):561–574, (1969).

[4] K. Iio, M. Sano, and K. Nagata. *J. Magn. Soc. Jpn.*, **11**(S1):59–62, (1987).

[5] F. J.Rioux and B. C. Gerstein. *J. Chem. Phys.*, **53**(5):1789, (1970).

[6] H. Nojiri, Y. Tokunaga, and M. Motokawa. *J. De Physique*, **C8**:1459, (1988).

[7] Y.Li, H. Liao, Z. Zhang, S. Li, F. Jin, L. Ling, L. Zhang, Y. Zou, L. Pi, Z. Yang, J. Wang, Z. Wu, and Q. Zhang. *Sci.Rep.*, **5**:16419, (2015).

[8] Y. Li, G. Chen, W. Tong, l. Pi, J. Liu, Z. Yang, X. Wang, and Q. Zhang. *Phys. Rev. Lett*, **115**:167203, (2015).

[9] Y. Shen, Y. D. Li, H. Wo, Y. Li, S. Shen, B. Pan, Q. Wang, H. C. Walker, P. Steffens, M. Boehm, Y. Hao, D. L. Quintero-Castro, L. W. Harriger, M. D. Frontzek, L. Hao, S. Meng, Q. Zhang, G. Chen, and J. Zhao. *Nature*, **540**:559–562, (2016).

[10] U. Geiser, H. H. wang, K. D. Carlson, J. M. Williams, Jr. H. A. Charlier, J. E. Heindl, G. A. Yaconi, B. J. Love, M. W. Lathrop, J. E. Schirber, D. L. Overmyer, J. Ren, and M. H. Whangbo. *lnorg. Chem.*, **30**(12):2586–2588, (1991).

[11] Y. Shimizu, K. Miyagawa, K. Kanoda, M. Maesato, and G. Saito. *Phys. Rev. Lett*, **91**(10):107001/1–107001/4, (2003).

[12] S. Yamashita, Y. Nakazawa, M. Oguni, Y. Oshima, H. Nojiri, Y. Shimizu, K. Miyagawa, and K. Kanoda. *Nat. Phys*, **5**:459–462, (2008).

[13] M. Yamashita, N. Nakata, Y. Kasahara, T. Sasaki, N. Yoneyama, N. Kobayashi, S. Fujimoto, T. Shibauchi, and Y. Matsuda. *Nat. Phys*, **5**:44–47, (2009).

[14] Y. Shimizu, T. Hiramatsu, M. Maesato, A. Otsuka, H. Yamochi, A. Ono, M. Itoh, M. Yoshida, M. Takigawa, Y. Yoshida, and G. Saito. *Phys. Rev. Lett*, **117**:107203, (2016).

[15] S. Yamashita, Y. Nakazawa, A. Ueda, and H. Mori. *Phys. Rev. B*, **95**:184425, (2017).

[16] R. Kato. *Bull. Chem. Soc. Jpn.*, **87**(3):355–374, (2014).

[17] K. Kanoda and R. Kato. *Annu. Rev. Condens. Matter Phys.*, **2**:167–188, (2011).

[18] S. Yamashita, T. Yamamoto, Y. Nakazawa, M. Tamura, and R. Kato. *Nat. Commun.*, **2**:275, (2011).

[19] M. Yamashita, N. Nakata, Y. Senshu, M. Nagata, H. M. Yamamoto, R. Kato, T. Shibauchi, and Y. Matsuda. *Science*, **328**:1246, (2010).

[20] 小形正男. *日本物理誌*, **69**:130–131, (2014).

[21] P. Pincus. *Solid State Commun.*, **9**:1971–1973, (1971).

[22] G. Beni and P. Pincus. *J. Chem. Phys.*, **57**(8):3531–3534, (1972).

[23] J. W. Bray, Jr. H. R. Hart, L. V. Interrante, I. S. Jacobs, J. S. Kasper, G. D. Watkins, H. Wee, and J. C. Bonner. *Phys. Rev. Lett*, **35**:744–747, (1975).

[24] C. L'huillier and G. Misguich. *cond-mat/0109146 lecture notes of the Cargese summer school on 'Trends in high magnetic field science'*, (2001).

[25] R. E. Dietz, F. R. Merritt, R. Dingle, D. Hone, V. G. Silbernagel, and P. M. Richards. *Phys. Rev. Lett*, **26**(19):1186–1188, (1971).

[26] M. Saito and H. Fukuyama. *J. Phys. Soc. Jpn.*, **66**(10):3259–3271, (1997).

[27] C. P. Nave and P. A. Lee. *Phys. Rev. B*, **76**:235124, (2007).

[28] O. I. Motrunich. *Phys. Rev. B*, **72**:2045105, (2005).

[29] M. Tamura and R. Kato. *Sci. Technol. Adv. Mater.*, **10**(2):024304/1–024304/12, (2009).

[30] R. Kato and H.-B. Cui. *Crystals*, **2**(3):861–874, (2012).

[31] R. Kato, T. Fukunaga, H. M. Yamamoto, K. Ueda, and H.-B. Cui. *Phys. Status Solidi B.*, **249**(5):999–1003, (2012).

[32] A. Rosa, G. Ricciardi, and E. J. Baerends. *Inorg. Chem.*, **37**:1368–1379, (1998).

[33] R. Kato. *Chem. Rev.*, **104**:5319–5346, (2004).

[34] M. Tamura and R. Kato. *J. Phys.: Condens. Matter*, **14**:L729, (2002).

[35] Y. Takano, K. Hiraki, R. Kato, and T. Takahashi. *Synth. Met.*, **135-136**:593–594, (2003).

[36] K. Otsuka, H. Iikubo, T. Kogure, Y. Takano, K. Hiraki, T. Takahashi, H. B. Cui, and R. Kato. *J. Phys. Soc. Jpn.*, **83**:054712/1–054712/6, (2014).

[37] T. Sakurai, H. Ohtab, S. Okubob, R. Kato, and T. Nakamura. *Synth. Met.*, **133–134**:421–422, (2003).

[38] T. Itou, A. Oyamada, S. Maegawa, M. Tamura, and R. Kato. *Phys. Rev. B.*, **77**:104413/1–104413/5, (2008).

[39] T. Itou, K. Yamashita, M. Nishiyama, A. Oyamada, S. Maegawa, K. Kubo, and R. Kato. *Phys. Rev. B.*, **84**:094405/1–094405/5, (2011).

[40] T. Itou, A. Oyamada, S. Maegawa, and R. Kato. *Nat. Phys.*, **6**:673, (2010).

[41] S. Fujiyama and R. Kato. *Phys. Rev. B*, **97**:035131, (2018).

[42] M. Tamura, A. Tajima, and R. Kato. *Synth. Met.*, **152**:397, (2005).

[43] A. Nakao and R. Kato. *J. Phys. Soc. Jpn.*, **74**:2754, (2005).

[44] R. Kato, A. Tajima, A. Nakao, and M. Tamura. *J. Am. Chem. Soc.*, **128**(31):10016–10017, (2006).

[45] M. Tamura, A. Nakao, and R. Kato. *J. Phys. Soc. Jpn.*, **75**(9):093701/1–093701/4, (2006).

[46] T. Itou, A. Oyamada, S. Maegawa, K. Kubo, H. M. Yamamoto, and R. Kato. *Phys. Rev. B*, **79**(17):174517/1–174517/1/6, (2009).

[47] R. S. Manna, M. Souza, R. Kato, and M. Lang. *Phys. Rev. B*, **89**:045113/1–045113/5, (2014).

[48] H. Ohta, S. Okubo, N. Souda, M. Tomoo, T. Sakurai, T. Yoshida, E. Ohmichi, M. Fujisawa, H. Tanaka, and R. Kato. *Appl. Mag. Reson.*, **35**(3):399–410, (2009).

[49] 山淳. *磁共鳴-ESR*. サイエンス社, (2009).

[50] Y. Oshima. *unpublished results*.

[51] P. W. Anderson. *J. Phys. Soc. Jpn.*, **9**(3):316–339, (1954).

[52] A. Abragam and B. Bleaney. *Electron Paramagnetic Resonance of Transition Ions*. Oxford University Press, Oxford, (2012).

[53] Z. H. Wang, E. M. Scherr, A. G. MacDiarmid, and A. J. Epstein. *Phys. Rev. B*, **45**(8):4190–4202, (1992).

[54] F. J. Dyson. *Phys. Rev.*, **98**(2):949–959, (1955).

[55] R. H. Webb. *Phys. Rev.*, **158**(2):225–233, (1967).

[56] M. Nishi, O. Fujita, and J. Akimitsu. *Phys. Rev. B*, **50**(9):6508–6510, (1994).

[57] L. P. Regnault, M. Ain, B. Hennion, G. Dhalenne, and A. Revcolevschi. *Phys. Rev. B*, **53**(9):5579–5597, (1996).

[58] R. E. Dietz, F. R. Merritt, R. Dingle, D. Hone, B. G. Silbernagel, and P. M. Richards. *Phys. Rev. Lett*, **26**(19):1186–1188, (1971).

[59] P. M. Richards. *Phys. Rev. B*, **10**(3):805–813, (1974).

[60] T. Takahashi, H. Doi, and H. Nagasawa. *J. Phys. Soc. Jpn.*, **48**(2):423–429, (1980).

[61] H. Tanaka, S. Kuroda, M. Mitsumi T. Yamashita, and K. Toriumi. *Phys. Rev. B*, **73**(24):245102/1–245102/12, (2006).

[62] K. Ueda, H. Kontani, M. Sigrist, and P. A. Lee. *Phys. Rev. Lett*, **76**(11):1932–1935, (1996).

[63] H. Kageyama, K. Yoshimura, R. Stern, N. V. Mushnikov, K. Onizuka, M. Kato, K. Kosuge, C. P. Slichter, T. Goto, and Y. Ueda. *Phys. Rev. Lett*, **82**(15):3168–3171, (1999).

[64] E. Pytte. *Phys. Rev. B*, **10**(5):2039–2043, (1974).

[65] M. Yamashita and H. Okamoto. *Material Designs and New Physical Properties in MX- and MMX-Chain Compounds*. Springer-Verlag, Wien, (2013).

[66] E. Canévet, B. Grenier, Y. Yoshida, N. Sakai, L. P. Regnault, T. Goto, Y. Fujii, and T. Kawae. *Phys. Rev. B*, **82**:132404/1–132404/4, (2010).

[67] T. Ohama, H. Yasuoka, M. Isobe, and Y. Ueda. *Phys. Rev. B*, **59**(5):3299–3302, (1999).

[68] H. Seo and H. Fukuyama. *J. Phys. Soc. Jpn.*, **67**(8):2602–2605, (1998).

[69] B. Grenier, O. Cépas, L. P. Regnault, J. E. Lorenzo, T. Ziman, J. P. Boucher, A. Hiess, T. Chatterji, J. Jegoudez, and A. Revcolevschi. *Phys. Rev. Lett*, **86**(26):5966–5969, (2001).

[70] T. Yamamoto, Y. Nakazawa, M. Tamura, A. Nakao, A. Fukaya, R. Kato, and K. Yakushi. *J. Phys. Soc. Jpn.*, **83**:053703, (2014).

[71] J. C. Bonner, J. A. Northby, I. S. Jacobs, and L. V. Interrante. *Phys. Rev. B*, **35**(4):1791–1798, (1987).

[72] Y. Inagaki, T. Kawae, N. Sakai, N. Kawame, T. Goto, J. Yamauchi, Y. Yoshida, Y. Fujii, T. Kambe, Y. Hosokoshi, B. Grenier, and J. P. Boucher. *J. Phys. Soc. Jpn.*, **86**(4):113706/1–113706/5, (2017).

[73] M. Hiraoka, H. Sakamoto, K. Mizoguchi, and R. Kato. *Phys. Rev. B*, **65**(4):174413/1–174413/4, (2002).

[74] T. Nakano and H. Fukuyama. *J. Phys. Soc. Jpn.*, **49**(5):1679–1691, (1980).